TECHNISCHE UNIVERSITÄT WIEN
Vienna University of Technology

DIPLOMARBEIT

Photoluminescence of plasmonically coupled silicon nanowires

ausgeführt zum Zwecke der Erlangung des

akademischen Grades eines Diplom - Ingenieurs

an der Technischen Universität Wien

Institut für Festkörperelektronik

unter der Leitung von

Ao.Univ.Prof. Dipl.-Ing. Dr.techn. Alois Lugstein

durch

Yasaman Hosseinnia, BSc

Matr.-Nr. 00126498

Wachtbergstrasse 9C/2

4852 Weyregg am Attersee

Wien, 06.05.2018

Statutory Declaration

I declare, that I have authored the present work independently according to the code of conduct, that I have not used other than the declared sources and that I have explicitly marked all material quoted either literally or by content from the used sources. This work was not yet submitted to any examination procedure neither in Austria, nor in any other country.

Erklärung zur Verfassung der Arbeit

Hiermit erkläre ich, dass die vorliegende Arbeit gemäß dem „Code of Conduct" Regeln zur Sicherung guter wissenschaftlicher Praxis, ohne unzulässige Hilfe Dritter und ohne Benutzung anderer als der angegebenen Hilfsmittel angefertigt wurde. Die aus anderen Quellen direkt oder indirekt übernommenen Daten und Konzepte sind unter Angabe der Quelle gekennzeichnet. Die Arbeit wurde bisher weder im In noch im Ausland in gleicher oder in ähnlicher Form in anderen Prüfungsverfahren vorgelegt.

Wien, 06.05.2018 ....

Yasaman Hosseinnia

Abstract

Being the key component of the semiconductor industry, silicon in form of nanowire has recovered increased attention. Semiconductors, especially silicon, form the basis of modern electronics, but, although silicon is the dominant semiconductor, light emitting devices are today based on semiconductors, which supports fast radiative recombination. Regrettably, silicon is owing to its indirect band gap an especially poorly emitter of light and is a kind of semiconductor, which converts extra energy into heat.

The problem is that silicon doesn't emit light and the materials that do it, are not absolutely the best materials for production electronic devices and are not compatible with silicon-based electronic devices. Thus integrating electronic and photonic circuits is a challenge. In an indirect band gap material like silicon, when the electron achieves the conduction band minimum, the valence band maximum does not match with corresponding moment. That is the main difference with a direct-band gap material. This prevents radiative recombination of the electron-hole pair from the conduction band minimum to the valence band maximum as both energy and momentum must be obtained.

Semiconductor nanowires are at the top of nanotechnology research. They combine the material properties of semiconductors with nanoscale dimensions. With silicon determined as the material of option for the electronics industry, improving its optical properties would make consumer-level usage of the technology more feasible. The aim of this work was thus to enhance light emission of silicon combining nanowires with plasmonics. Using silicon nanowires and metallic nanocavities leads to increased interaction between light and matter. This interaction arises when light is confined to dimensions below the size of its wavelength.

This thesis examines how the integration of plasmonic cavities and semiconductor nanowires leads to essential increase of efficient visible light emission that may be tuned as a function of cavity geometry and the used materials. The purpose is the verification and optimization of a method in order to achieve the highest possible photoluminescence.

To generate light emission from hot carriers, a plasmonic nanocavity on individual silicon nanowires was fabricated by depositing an oxide interlayer followed by the formation of a silver cavity to support surface plasmon polariton modes.

Once the electron is excited to the conduction band in silicon, characteristically by a phonon assisted process, its behavior is similar to that of an excited charge carrier in a semiconductor with a direct band gap. The excited electron will rapidly rest up to the conduction band minimum via phonon scattering events. To understand the cooperation of silicon phonon and nanocavity plasmon resonances leading to efficient light emission, photoluminescence (PL) measurements were carried out. The result of this experiment was broadband luminescence from silicon nanowires.

The experimental observations can also be explained by the Purcell effect. Purcell effect describes that the rate of light emission from an electron-hole pair in a semiconductor is a function of the environs of that optical emitter. The use of optical cavities to enhance the spontaneous emission rate of excited atoms is discussed according to the Purcell theory.

The focus of this work is to obtain spontaneous emission enhancement using plasmonic nanocavities. Additional, characteristics of surface plasmon polaritons (SPP) are described. Metals can confine the light in to deep-subwavelength dimensions. When light is invading on the surface of a metal the surface electrons and photon may form a strongly coupled system, known as the surface plasmon polariton. The surface electrons embed the light to the surface of the metal. This results in an electromagnetic mode that may propagate on the surface of the metal.

Finally silicon nanowires coupled with plasmon nanocavities were integrated in an electrostatic actuated straining device (EASD) and the changes in PL spectra depending on strain were investigated. Silicon strain engineering is an essential process innovation in semiconductor fabrication. The piezoresistive effect is a change in the resistance of a semiconductor or metal when a strain is applied. The piezoresistivity of silicon is ten to twenty times higher than in metals. Silicon is therefore a promising alternative for strain gauges with high sensitivity. This knowledge made silicon a promising alternative for strain gauges with high sensitivity. On the other hand, nanowires exhibit a giant piezoresistivity and thus can be used to enhance the strain sensitive sensors. In this work it is attempted to combine this advantage of silicon nanowires with plasmonics and to observe the PL effects in nanowires as a function of strain.

Kurzfassung

Silizium gilt seit vielen Jahrzehnten als ideales Ausgangsmaterial für die Halbleiterindustrie. Silizium hat viele Vorteile gegenüber anderen Halbleitern und eignet sich hervorragend für elektronische Bauelemente, aber für Optoelektronik und als Lichtemitter ist es aufgrund seiner indirekten Bandlücke und besonderen elektronischen Struktur nicht einsetzbar.

Lichtemission in Halbleitern findet allgemein durch die Rekombination eines Elektrons aus dem Leitungsband mit einem Loch aus dem Valenzband des Halbleiters statt. Die Wahrscheinlichkeit für eine Rekombination unter Emission eines Photons ist in direkten Halbleitern sehr hoch. Für diesen Prozess muss sowohl die Energieerhaltung als auch die Impulserhaltung gelten. Das Minimum des Leitungsbandes und das Maximum des Valenzbandes liegen in indirekten Halbleitern bei unterschiedlichen Quasiimpulsen (Wellenvektor). Aus diesem Grund ist sowohl ein Photon als auch ein Phonon erforderlich. Daher sind die nichtstrahlenden Rekombinationen in indirekten Halbleitern der dominierende Rekombinationsmechanismus und aus diesem Grund die Lichtemission sehr ineffizient.

Halbleiter-Nanodrähte kombinieren die Materialeigenschaften von Halbleitern mit Nanometerdimensionen. Verbesserte optische Eigenschaften in Silizium-Nanodrähten öffnen ein Fenster, um nicht nur die bestehenden Bauteile für photonische und optoelektronische Zwecke zu verbessern, sondern auch neue Bauteile zu realisieren.

Der Fokus dieser Masterarbeit liegt daher auf plasmonisch gekoppelten Halbleiter-Silizium-Nanodrähten. Es wird untersucht, wie die Integration plasmonischer optischer Resonatoren und Silizium-Nanodrähten zu einer wesentlichen Steigerung der Emission von sichtbarem Licht führt. Ziel ist die Herstellung von plasmonisch gekoppelten Silizium-Nanodrähten mit stark verbesserten optischen Eigenschaften im Vergleich zu Bulk-Silizium.

Um effektive Lichtemission von Nanodrähten zu erzielen, wurde ein plasmonischer Nanoresonator auf einzelnen Silizium-Nanodrähten hergestellt, indem eine Oxidzwischenschicht abgeschieden wurde, gefolgt von einer Silberschicht.

Das angeregte Elektron im Leitungsband bewegt sich über Phononenstreuung schnell bis zum Leitungsbandminimum. Die Kooperation zwischen Phonon und Nanokavität Plasmonen führt zu einer effizienten Lichtemission. Um diesen Prozess zu beobachten, wurden Photolumineszenz (PL)-Messungen durchgeführt. Mit solchen plasmonisch gekoppelten Silizium-Nanodrähten konnte breitbandige Lumineszenz im Bereich von 550 nm bis 750 nm also im Sichtbaren erzielt werden.

Die experimentellen Beobachtungen lassen sich mit dem Purcell-Effekt erklären. Der Purcell-Effekt beschreibt die Änderung der spontanen Emission eines Emitters in der Umgebung einer modifizierten optischen Zustandsdichte. Es wird versucht eine hohe Verstärkung der spontanen Emission mit plasmonischen Nanokavitäten zu erreichen. Kollektive Oszillationen der freien Leitungselektronen im Metall können diesen Verstärkungsmechanismus erklären. Licht kann sich an der Grenzfläche zwischen einem Metall und einem Dielektrikum durch kollektive Oszillationen der freien Elektronen im Ladungsträger ausbreiten. Die sogenannten Oberflächenplasmonen führen dazu, dass das elektromagnetische Feld des Lichts an der Oberfläche konzentriert wird. Für die Steuerung und

gezielte Anwendung dieser plasmonischen Effekte müssen Strukturen in der Nanometergröße hergestellt werden, um resonant mit dem Licht interagieren zu können.

Anschließend wurde das gleiche Prinzip verwendet, um die plasmonisch gekoppelten Silizium-Nanodrähte auf einer elektrostatisch aktuierten Verdehnungseinrichtung (EASD) herzustellen. Änderungen der PL-Spektren in Abhängigkeit von der mechanischen Verspannung der Nanodrähte wurden gemessen und diskutiert. „Strain engineering" in Silizium ist eine wesentliche Prozessinnovation in der Halbleiterherstellung. Der piezoresistive Effekt beschreibt die Widerstandsänderung eines Halbleiters oder eines Metalls unter Verspannung. Die Piezoresistivität von Silizium ist zehn bis zwanzigfach höher als in Metallen. Silizium ist daher eine viel versprechende Option als Dehnungsmesser mit hoher Sensitivität. Andererseits zeigen Nanodrähte die abnormale und große Piezoresistivität und daher werden sie zum Verbessern der dehnungssensitiven Sensoren verwendet.

Diese Arbeit behandelt allgemein die Untersuchung und Optimierung der beschriebenen Technik um ein möglichst hohes PL Spektrum zu erzielen und dabei wurde beobachtet, wie die Integration von plasmonischen Nanoresonatoren und Silizium-Nanodrähten zu einer wesentlichen Steigerung der Emission von sichtbarem Licht führt. Es sollten diverse Möglichkeiten in Betracht gezogen werden, um die PL Spektren der plasmonisch gekoppelten Silizium Nanodrähte gezielt zu beeinflussen.

Danksagung

Contents

1. Introduction

The constantly increasing requirement for rapid transport of information and processing capabilities is incontrovertible. Our society has become hungry for data, which led to a tremendous progress in the silicon electronics industry. Over the past fifty years, the world has a continuous development towards more efficient, smaller and faster electronic devices. The scaling of these devices has also brought to innumerable of challenges. [1]

At the present time, two of the most serious problems preventing essential increases in processor speed above 10 GHz are thermal and RC delay time issues with electronic cross-linking. [2]

Optical interconnects do not face these problems and demonstrate a nearly inconceivable significant data- carrying capacity. Silicon has emerged as the dominant material of choice for the electronics industry, increasing its optical attributes so to be assimilated into photonic circuitry would make consumer-level applications of the technology much more practical and feasible. [3] A reduction in size of dielectric waveguides is unfortunately limited basically by the diffraction limit of light, imposing a lower size limit on a guided light mode of about $\lambda/2n$.

However, the photonic structures are showing a tendency to still be at least 1 or 2 orders of magnitude larger than their electronic counterparts. This obvious mismatch of sizes between electronic and photonic components has demonstrated crucial problems in interfacing these technologies, creating a barrier that prevents higher data processing speeds. Therefore it is likely that further progress will require the development of a fundamentally new device technology that could make an easier transport of information between nanoscale devices at optical frequencies and build a bridge between the world of electronics and photonics. [4]

A candidate technology has recently been explored and has been termed "plasmonics" [1], which will be discussed in this thesis.

With a view to achieving ultrafast optical data processing there have been several studies on silicon optoelectronics in order to approach the limitations in device speed and performance in silicon-based electronics. [5]

There are a few systems, which could route data optically between processors at high speeds, overcoming a narrow bandwidth launched by the physical limitations of copper interconnect. [6] Dissimilarly photonics based on III-V semiconductors, such as gallium arsenide or indium phosphide, silicon photonics would depend on the same CMOS manufacturing processes used to make other chip components, which would be cheaper while avoiding the incompatibilities of different materials.

The most serious challenge is that silicon really does not tend to emit light because, unlike gallium arsenide and indium phosphide, it has an indirect bandgap, which means the minimum energy in the conduction band and the maximum energy in the valence band occur at different values of electron momentum. Only if a source of momentum of just the right scale, such as a vibration in the crystal lattice, phonon, is present an electron in the conduction band can recombine with a hole in the valence band to produce a photon. [7] That means excited electrons and holes are more suitable to emit heat than light when they recombine. [6]

The researchers have tried to solve the problem by doping silicon with other materials but the light emission is in the very long wavelength range degrading its electronic properties. [8] Another scheme is based on a curious effect called "quantum confinement". That results when an electron-hole pair is physically limited to a small area. When a bulk semiconductor is reduced in size to a nanosized semiconductor, the bandgap moves to larger values because of the quantum confinement of excitons into more discrete energy levels rather than continuous bands. [9]

Especially, the efficient visible luminescence from porous silicon brings notable experimental studies in nano-dimensional silicon materials, because the PL efficiency of porous silicon is very high and very large porous layer can be fabricated on crystalline silicon wafer. [10] Following the discovery that highly porous material could emit very efficient visible photoluminescence at room temperature much progress has been made in this field. [11]

The finding of visible luminescence from silicon nanostructures opens a new chance for the use of the indirect bandgap semiconductors as materials for optoelectronic applications. [9] These described effects allow the device to emit light, but making electrical connections at that scale is not currently feasible and would lead to very low electrical conductivity. In order to solve that problem, it will be turned to the plasmonic effect.

Plasmonic is an evolutional section of research that opens the rout for controlling light-matter interactions on the subwavelength scale, enabling the nanophotonic technologies that are unachievable with conventional optical components. [8] Plasmonic allows the changes in the flow of light in a nanometer scale (well below the diffraction limit), by exploiting the unique optical properties of metallic structures. [12]

This thesis describes a new method to achieve visible light emission from bulk-sized silicon combined with a plasmon nanocavity and examines how the integration of plasmonic cavities and semiconductor nanowires leads to essential increase of efficient visible light emission. These may be tuned as a function of cavity geometry and the used materials. The purpose is the verification and optimization of a method in order to achieve the highest possible photoluminescence.

The ability to navigate and manipulate the optical properties in semiconductor nanowires, through strain engineering, has important signification for the design of future optical devices. Generally, when the diameter of the nanowires reduced, then the strain on the crystallographic structure of the nanowire increased, yielding in a shift in the PL maximum to higher energies. [13] An attempt is to combine the plasmonic effects with strain and to investigate the influence of strain on PL.

2. Theory

The first part of this chapter is focused on the properties of silicon, as the main material used for this work.

After the description of the physical and particularity electronical and optical properties of silicon, a short overview is given about a luminescence effect namely photoluminescence. Further the basic theory of plasmonics is described. In the last chapter, the theory of microresonators and Purcell effect will be presented.

2.1 Semiconductor silicon

Crystalline silicon (c-Si) is an essential material that has been the basis of the semiconductor industry and has led to extraordinary technological advancement. In recent years, nanostructured silicon has been received great attention and interests in different experimental and theoretical fields. It is not only important for a variety of optical and electronic devices, but it is also easy to integrate into smaller modules. [14]

2.1.1 Basic characteristics

Berzelius has prepared "elemental silicon" for the first time in 1823. He placed silicon tetrafluoride in the presence of warm potassium. However it was thought that Gay-Lussac and Thenard had already obtained the amorphous silicon by the same method, in 1809. The material obtained by Berzelius was a purer product as a result of exhausting filtering. [15] Henri Étienne Sainte-Claire Deville was the first person who prepared crystalline silicon in 1854. [16]

The crystal structure of silicon is denoted as diamond structure and is illustrated in figure 2.1. The lattice constant of silicon, that is the distance between two atoms on the edges of the unit cell is 5.43095 Å. Having the four valence electrons is representing silicon as a tetravalent material. The outermost electron shell of each atom can accommodate up to eight electrons and the atom is most stable when the shell is completely populated. In a crystal of pure silicon, each atom has a part-share in eight valence electrons. This arrangement is a very stable one, which is also found in other materials like germanium (Ge) and the eponym diamond. [16]
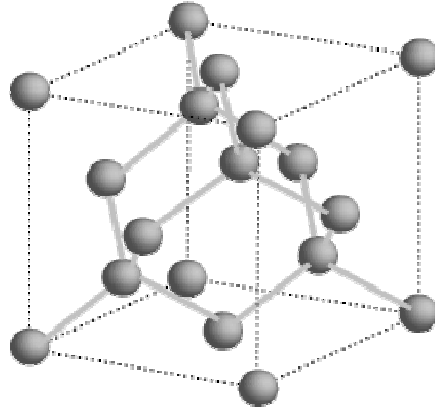
Figure 2.1: Schematic illustration of the diamond cubic crystal structure of silicon.

For an overview, the most important properties of intrinsic Si are listed in table 2.1.

Table 2.1: Properties of intrinsic silicon at room temperature

Properties	
Atoms/cm^3	$5.0 \cdot 10^{22}$
Lattice structure	diamond
Density (g/cm^3)	2.328
Lattice constant (Å)	5.43095
Melting point (°C)	1415
Bandgap (eV) at 300K	1.12
Intrinsic carrier concentration (cm^{-3})	$1.45 \cdot 10^{10}$
Intrinsic resistivity ($\Omega \cdot$ cm)	$2.3 \cdot 10^5$
Effective mass of electrons m*$_n$/m$_0$	m*$_l$: 0.98 , m*$_t$: 0.19
Effective mass of holes m*$_p$/m$_0$	m*$_{lh}$: 0.16, m*$_{hh}$: 0.49
Electron mobility (cm^2/V s)	1500
Hole mobility (cm^2/V s)	450
Minority carrier lifetime (s)	$2.5 \cdot 10^{-3}$
Critical field (V/cm)	$\approx 3 \cdot 10^5$
Dielectric constant	11.9

m*$_l$ longitudinal, m*$_t$ transverse
m*$_{lh}$ light hole, m*$_{hh}$ heavy hole

Bulk silicon is known as an indirect bandgap semiconductor. The band structure, which is show in figure 2.2, is an indirect semiconductor. The minimum of the conduction band is not located above the maximum of the valence band in k space, which confirms that the recombination of an electron in the conduction band with a hole in the valence band requires that a third particle (phonon) is present in order to compensate for the change in quasiimpulse. The eventuality of coincidence of three particles with 'suitable' properties is much lower than the coincidence of only two such particles, which is an adequate condition for recombination in direct bandgap semiconductors. It shows that the probability of electron transitions accompanied by the emission of a photon is significantly lower in indirect bandgap semiconductors than in direct bandgap ones, making, in most cases, the direct bandgap semiconductors the candidates of choice for light emitting devices.
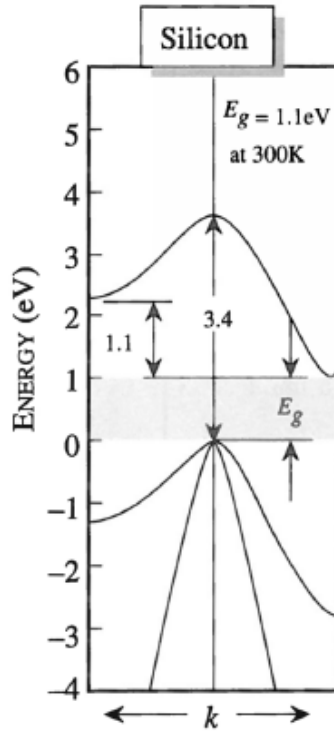
Figure 2.2: Band structure of crystalline silicon [17]

2.1.2 Silicon nanowire growth

Silicon nanowires are known as promising materials that have been gaining a lot of attention for their specific applications such as field-effect transistors, nanobiosensor [18] and solar cells [19].

Wagner and Ellis introduced the vapor-liquid-solid (VLS) mechanism in 1964, which is one of the most common ways to synthesize single crystalline silicon nanowires. Whereas the first grown wires had micrometer scale, Westwater et al. presented in 1997 the synthesis of VLS grown silicon nanowires at nanometer scale. [20] Figure 2.3, shows schematically the VLS growth technique which consists basically of three stages.

Figure 2.3: VLS synthesis of silicon nanowires
a) The gold catalyst is positioned on the silicon substrate; b) the silane precursor gas is decomposed on the gold droplet surface c) due to a supersaturation of silicon, a precipitation of crystalline silicon at the liquid/solid interface leads to an axial growth of the silicon nanowire

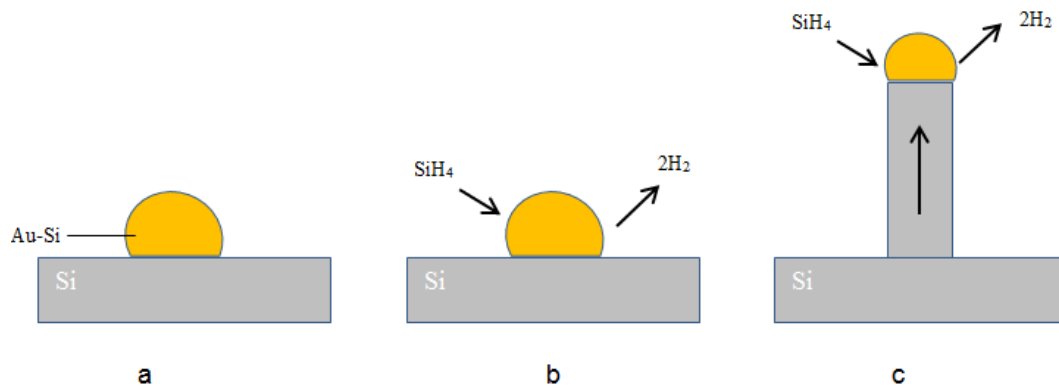The VLS mechanism is requiring nanosized metal particles catalyzing the quasi 1D growth of silicon nanostructures. Gold is known as the most common catalyst material, which is used for silicon nanowire synthesis using the VLS mechanism. The catalyst in form of a thin gold layer is deposited on the silicon substrate surface and will be melted at the growth temperature and forms nanosized droplets to minimize their surface energy. Nanosized collide particles can be directly deposited on the substrate surface as a second alternative (figure 2.3.a). The metal particles become liquid at the increased growing temperatures.

A semiconductor material containing precursor gas e.g. silane (SiH_4) will be inserted after heating up the substrate inside a low pressure chemical vapor deposition (LPCVD) reactor. The precursor gas represents the vapor phase of the semiconductor in VLS mechanism. The silane get decomposed at the catalytic gold droplet surface. Silicon atoms get absorbed and the excess hydrogen evaporates and will be pumped out of the LPCVD chamber (figure 2.3 b). The semiconductor material forming a liquid-alloy with the Au particle is representing the liquid term of the VLS mechanism in this phase. The silicon content inside the liquid gold droplet increases until it supersaturates. Crystalline silicon will precipitate, due to the supersaturation, at the droplet/substrate interface lifting the droplet and shaping a silicon nanowire (figure 2.3 c), which represents the solid term of VLS. [21]

2.1.3 Electrical properties of the semiconductor silicon

In this part of chapter 2 basic semiconductor physics is considered with special attention to silicon. As described in section 2.1.1, silicon is an indirect semiconductor. Inside the band gap, between the conduction band and the valence band, exist no energy states which can be occupied by electrons. Thus the electrons are situated in the conduction band and in the valence band. The amount of possible electron states per energy level in the bands is given by the density of states $N_e(E)$. Next to free energy states, a probability that this states are occupied have to be given for the existence of electrons at a certain energy level. The occupancy is dependent on temperature and is represented by the Fermi-Dirac distribution function f(E). The energy, at which the probability for electron occupancy of 50% is

given, is called Fermi level E_f. [17] The function f(E) represents the occupation probability of a state of energy E by an electron and given by:

$$f(E) = \frac{1}{1 + e^{(E - E_f)/kT}}$$

Density of states as well as occupation probability in intrinsic silicon is illustrated in figure 2.4. [17]
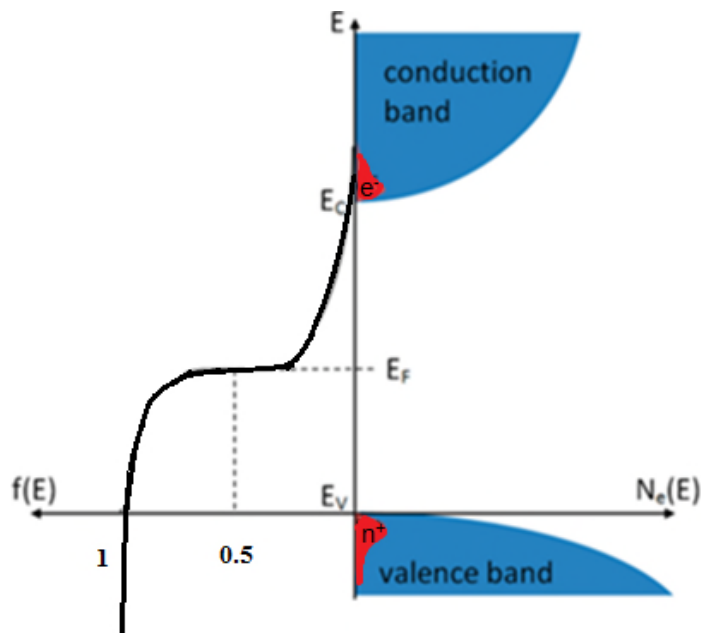
Figure 2.4: Depiction of the density of states (blue) and the occupation probability for an intrinsic semiconductor (red) [21]

For energy levels in the conduction band where the density of states as well as the occupation probability are not zero, the red marked energy states in figure 2.4 are occupied with free electrons. Pure elemental semiconductors have equal numbers of electrons and holes because every electron that is thermally excited to the conduction band leaves behind a hole in the valence band. [22]

Electrical current can be carried either by electrons (conduction band) or by holes (valence band). The conduction band electrons are delocalized over the entire crystalline solid, as in metals. However, the valence electrons are associated with specific covalent bonds, so electrical conduction by holes

requires electrons from an adjacent covalent bond to hop into an empty hole. A coordinated series of such hops in the direction of the applied electric field will carry electrical current.

The hopping of electrons to fill holes is similar to the hopping of atoms to fill vacancies during solid-state diffusion. Although the species moving are actually electrons, this is easier to visualize as hopping of the holes in the opposite direction. The electrical conductivity of an intrinsic semiconductor is given by:

$$\sigma = n.|e|.\mu_e + p.|e|.\mu_h$$

Where n is the electron concentration, p is the hole concentration, and μ_e and μ_h are the electron and hole mobility, respectively. However, each thermal activation event produces one electron and one electron hole, so for an intrinsic semiconductor: $n = p = n_i$

Additionally, the same absolute value of the charge is carried by each of these carriers:

$$\sigma = n_i|e|.(\mu_e + \mu_h)$$

Figure 2.5 shows the intrinsic carrier concentration of some semiconductors as a function of the temperature. This is plotted in log scale, since it follows an Arrhenius type equation:

$$n_i \propto \exp(-E_g/2kT)$$

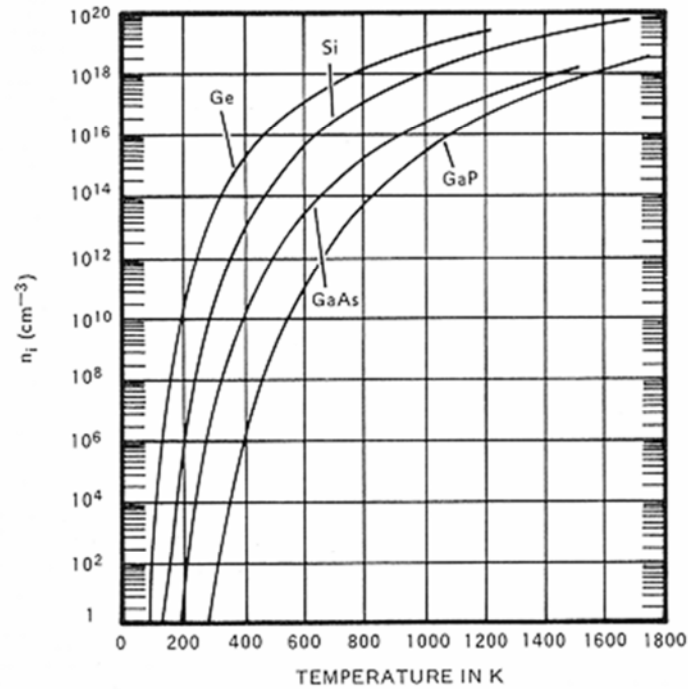With $E_g = E_c - E_v$ the energy bandgap. [23]

Figure 2.5: Intrinsic carrier densities of Ge, Si, GaP and GaAs as a function of temperature [23]

Pure semiconductor materials with large bandgap exhibit relatively low conductivities but the utility of these materials is that the electrical properties can be modified drastic by the introduction of impurities. The electrical characteristics of silicon can be changed through doping. Doping means the introduction of impurities into a semiconductor crystal to the defined change of conductivity. The most important materials silicon can be doped with, is boron, aluminum, indium (3 valence electrons) and phosphorus, arsenic, antimony (5 valence electrons). [24]

When a 3-valent dopant with its three valence electrons replaces a silicon atom, it can catch an additional outer electron. That means an additional electron is "accepted" to form four covalent bonds around the dopant, thus leaving a hole in the valence band of silicon atoms. Therefore the electrons in the valence band become mobile. Such dopants are called acceptors and the doping with them forms a p-type semiconductor. When a 5-valent dopant is added to silicon, the dopant with its five valence electrons forms covalent bonds with its four neighboring silicon atoms. Four outer electrons combine with ever one silicon atom, while the fifth electron is free to move. The dopant is called a donor and silicon is referred to as an n-type semiconductor. [25]

Figure 2.6 shows the energy difference between the conduction band and the valence band. This energy difference is called the band gap.

9
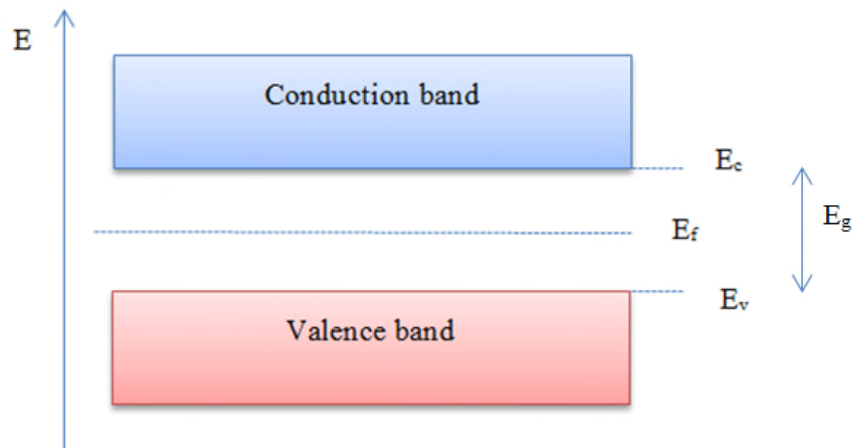
Figure 2.6: Fermi level (E$_f$) for the intrinsic semiconductor in the middle of forbidden band (E$_g$). In intrinsic semiconductors, the number of holes in the valence band has to be the same as free electrons in the conduction band

The exponential increase in carrier concentration with temperature causes a corresponding raise in the conductivity with temperature for an intrinsic semiconductor, but it should be considered that the carrier mobility is typically reduced as the temperature increases.

Semiconductors with large band gap contain a lower intrinsic carrier concentration. Increasing the temperature increases the number of electrons excited into the conduction band and therefore rises the carrier concentration.

The Fermi energy of an intrinsic semiconductor is given by:

$$E_f = \frac{E_v + E_c}{2}$$

This means that the Fermi level of an intrinsic semiconductor is located to the center of the bandgap. [24]

$$E_f = E_v + \frac{E_g}{2}$$

2.1.4 Optical properties of the silicon

The nature of the band gap has important impact on the optical properties of a semiconductor. The band gap describes the minimum energy difference between the top of the valence band and the bottom of the conduction band. Generally, there are two kinds of band structure, direct (a) and indirect (b) bandgap (as shown in figure 2.7).
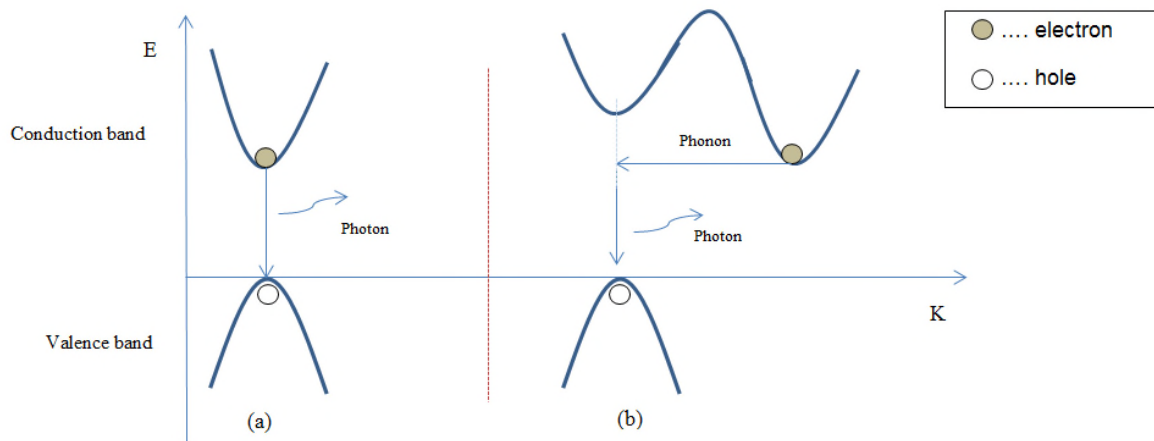
Figure 2.7: Scheme of optical transition in semiconductors with a (a) direct bandgap and (b) indirect bandgap.

A direct band gap means that the minimum of the conduction band is directly located above the maximum of the valence band in the E(k) diagram. In contrast, in the indirect band gap material the highest energy of the valence band and the lowest energy of conduction band occur at a different momentum. The difference between the two types of material is most important for optical devices.

A photon can provide the energy to produce an electron-hole pair. Each photon of energy E has momentum:

$$p = \frac{E}{c}$$

Where c is the velocity of light and E is the energy of photon. An optical photon has a very small amount of momentum. In the direct band gap material, a photon of energy E_g, can produce an electron-hole pair easily because the electron does not need to be given very much momentum. In indirect band gap material, an electron must experience a great change in its momentum for a photon of energy E_g to produce an electron-hole pair. However, the optical photon does not have enough momentum to allow the transition from conduction band to valence band itself.

But, this can achieve when the electron interacts not only with the photon to obtain energy, but also with a lattice vibration called a phonon in order to either gain or lose momentum. The process of indirect absorption is called a second order process because two quasi particles (a photon and a phonon) are involved and the absorption coefficient is calculated using second order perturbation theory. Therefore, the indirect process proceeds at a much slower rate.

The same principle counts for emission of light via recombination of electrons and holes. The recombination process is much more efficient for a direct band gap material than for an indirect band gap material, where the process must be again supplied by a phonon. [26]

As previously discussed, silicon is an indirect band gap semiconductor. The bandgap of silicon gives rise to extremely low emission efficiencies. The band structure of silicon is shown in figure 2.8.

If light with energy $h\nu > E_g$ is incident on a semiconductor it can be absorbed, exciting an electron to the conduction band and leaving a hole in the valence band. The electron in the conduction band and the hole in the valence band are called an electron hole pair. After the electron hole pairs are generated, they may recombine in order to obtain a lower energy state. This recombination can appear via a diversity of paths, the simplest of which is band-to-band recombination.
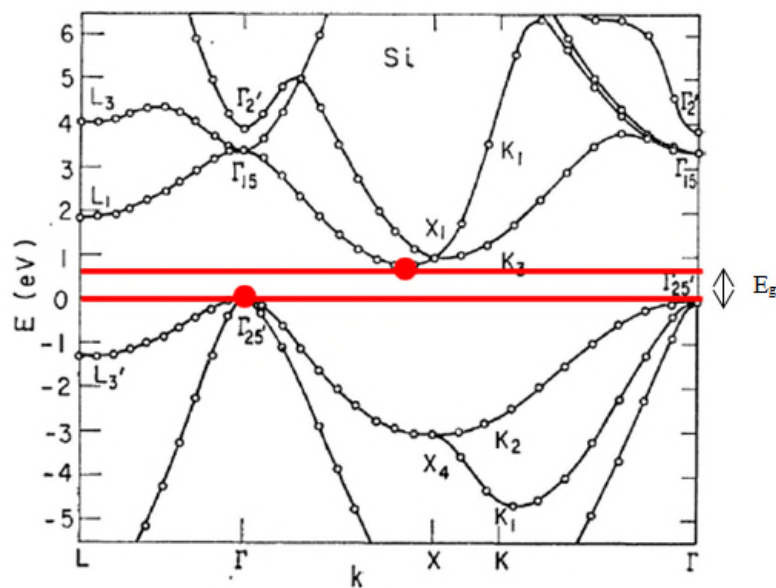
Figure 2.8: The band structure of silicon [27]

As the electron makes the transition from the conduction band to a state within the forbidden band, it loses energy. The energy must be transmitted to some other particle, typically either a photon or a phonon. Transitions that emit photons are referred to as radiative processes, and transitions that generate only phonons are nonradiative processes. There are transitions, which include both phonon, E_{ph}, and photons, h.ν, as it is the case by radiative band-to-band transition in silicon. The energy of the resulting photon is given by: [28]

$$h\nu = E_g - E_{ph}$$

Development of an efficient silicon-based light source is a big challenge, because the indirect bandgap of silicon gives rise to extremely low emission efficiencies. [5]

2.2 Luminescence

Luminescence is defined as the emission of light not resulting from heat that occurs when a system makes a transition from an electronically excited state to a lower energy state (the ground state). It is thus the process of light emission by a solid when given some form of energy, which can be provided by different methods depending on the excitation process: [29]

- Photoluminescence (PL): excitation comes from absorption of photons (e.g. glow in the dark paint).

- Cathodoluminescence (CL): this form of luminescence is generated by phosphor excitation due to bombardment by an electron beam (e.g. old types of displays for TVs and desktop computers).

- Electroluminescence (EL): excitation by applying an electric field and injection of charge carriers (electrical current). This capability is useful as a basic technique for the new generation of LED and OLED TVs and monitors.

The reason of luminescence in solid material is an "excitant" that increase the energy level of the material and the extra energy is given off as visible light. [30]

The final step is an electronic transition (independently from the source of excitation) between two states of energy E_1 and E_0 with emission of a photon of a specific wavelength and color that depends on the energy levels.

$$h.\nu = E_1 - E_0 = h.c/\lambda$$

$E_1 - E_0$ is the difference in energy from the excited state to a lower state. A more detailed discussion of PL is given in the following section.

2.2.1 Photoluminescence

As already described, luminescence is the phenomenon in which electronic states of solids are excited by some energy $h.\nu > E_g$ from an external source and the excitation energy is released as light. When the energy comes from the light, normally ultraviolet light, the phenomenon is called photoluminescence. [31]

Photoluminescence is categorized in two different classes:

- intrinsic luminescence

- extrinsic luminescence

Intrinsic luminescence is further classified as 3 individual types:

1- Band-to-Band luminescence

2- Exciton luminescence

3- Cross-luminescence

Band-to-Band luminescence: A photon with an energy larger than the band gap E_g of a particular semiconductor excites an electron from the valence band into the conduction band (figure 2.9.a). Therefore an electron-hole pair is created and the electron due to thermalization moves to the bandgap minimum. Direct bandgap semiconductor materials do not need a change in crystal momentum for absorption and emission processes, so that band-to band transition is possible without participation of a phonon (figure 2.9.b). Band-to-band luminescence can be observed in very pure crystals at relatively high temperatures. [32]

For Si, Ge or other indirect semiconductors, the minimum of the conduction band and the maximum of the valence band are not positioned at the same k values and due to this reason; a transition is possible only as a result of the interactions with phonons. This obvious fact makes absorption and emission of photons much more unlikely in indirect semiconductors. [33]
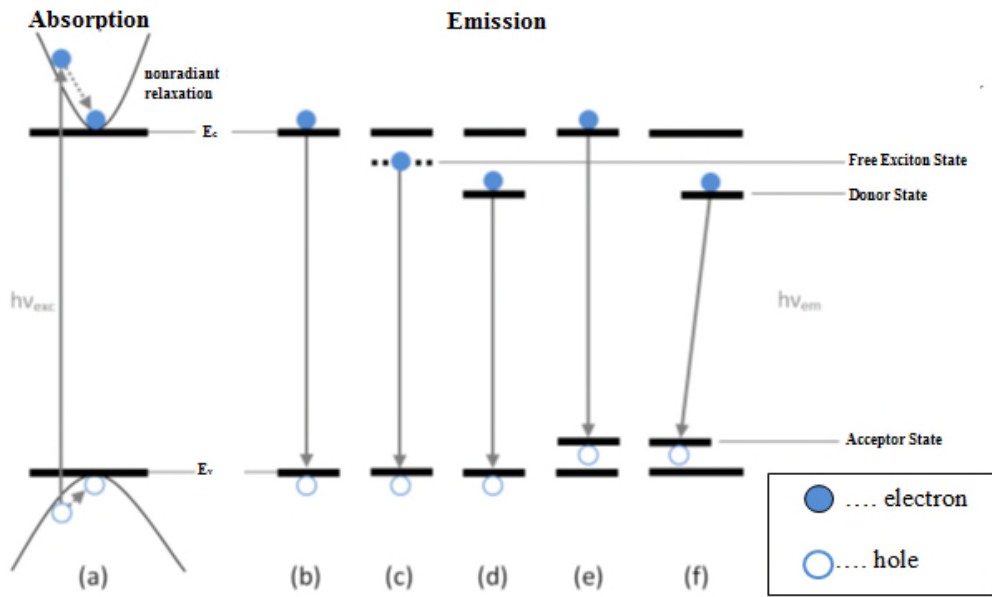
Figure 2.9: Schematic of the mechanism of absorption and emission in semiconductors (a) Absorption by band-to-band transition, following thermalization of the carriers to the bandgap minimum. Photoluminescence occurs due to (b) band-to-band transition, (c) excitonic recombination, (d) and (e) recombination of unlocalized type involving one defect level and (f) donor-acceptor-pair luminescence [33]

Exciton luminescence: An exciton is a quasiparticle, which consists of an electron in the conduction band and a hole in the valence band bound with the electrostatic Coulomb force. Therefore this particle is capable to convey energy in a crystal without transferring a net charge. Only if the binding energy is higher than the thermal energy, excitons are assumed to be stable, which is taking place at very low temperatures. Radiation which consists of very sharp lines is emitted after recombination of the exciton electron and hole recombination (figure 2.9.c). Therefore the excitons containing a distinct energy $E_{ex} = E_g - G_{ex}$, where G_{ex} is the binding energy of the exciton. If there are some impurities included in the crystal lattice, excitons can be bound to them, whereby the exciton lines of the luminescence spectrum are shifted towards lower energies (figure 2.9.d).

Cross-luminescence: it is generated as another form of luminescence by recombination of an electron in the valence band with a hole created in the outermost core band. This kind of luminescence is observed in a number of alkali, alkaline-earth halides and double halides. [32]

Extrinsic luminescence is classified in 2 individual types:

Unlocalized type: The formation of impurity energy levels is originating from the introduction of impurities into a semiconductor. These levels are effective traps for carriers which may act as luminescence activators. After the band-to-band excitation by absorption of a photon, holes may drift to the luminescent center where they recombine with electrons of the defect level, whereas this level is filled by an electron of the conduction band subsequently. This mechanism is possible for donor states (figure 2.9.d) as well as for acceptor states (figure 2.9.e). Another luminescent mechanism in semiconductors is the donor-acceptor-pair luminescence. This type of process is supposable in III-V or II-VI semiconductors with amphoteric dopants, i.e. GaAs doped with Si.

Under these circumstances, the radiation emerges by recombination of an electron in the donor level with a hole in the acceptor level (figure 2.9.f). A radiationless recombination through these levels is highly probable, if too different impurity energy levels are introduced into a semiconductor or the defect levels are very close to the gap center. [33]

Localized type: Extrinsic luminescence of localized type is led back to the impurities themselves. This luminescence mechanism is bordered in a localized luminescence center where both, absorption and emission happen. An excitation of the electronic states of an incorporated atom or a molecule occurs by absorption of a photon. By releasing the excitation energy, luminescence is created. [32, 34]

2.3 Plasmonics

Investigations in the field of optical phenomena related to the electromagnetic response of metals, led to the development of an emerging and fast growing research field of called plasmonics.

The term "plasmonics" is derived from the electron density waves that propagate along the interface of a metal and a dielectric like the ripples that spread across a water surface after throwing a stone into the water. [35]

Plasmonics shows how light can be conducted along metal surfaces or within nanometer-thick metal films. The principle of plasmonics is defined on an atomic level where metal crystals have a very organized lattice structure. The lattice contains free electrons, not closely associated with the metal atoms, which interact with the light that hits them. These free electrons collectively start to oscillate with respect to the fixed position of positively charged nuclei in the metal lattice. The electron density fluctuates in the metal lattice as a plasmon wave closely similar to that of the density of air molecules in a sound wave. Visible light has a wavelength of approximately half a micrometer and therefore it can be concentrated by a factor of nearly 100 to travel through metal films just a few nanometers thick. Such mixed light-electron-wave-state empowers intense light-matter interactions with unprecedented optical properties. [36]

There are two types of plasmons; bulk plasmons and surface plasmons. In the following, the basic physical concepts of plasmonics are described and the main fields of application will be presented.

2.3.1 Bulk plasmons

Bulk plasmons are the most fundamental and intrinsic type of a plasmon resonance that can be supported by a metal. These resonances exist at the plasma frequency of metals ω_p, which are transparent to radiation with higher frequencies and non-transparent to radiation with lower frequencies. The plasma frequency mainly depends on the electron density of the material and defined as:

$$\omega_p{}^2 = \frac{Ne^2}{\varepsilon_0 m}$$

In which N is the free electron charge density of the metal, e and m are the electron charge and mass respectively and ε_0 is the permittivity of free space (8.854×10^{-12} F/m). These bulk plasmons are longitudinal modes which cannot be excited by an incident photon, but rather by particle impact.

Due to the large values of electron density (N ~10^{28} m^{-3}), the plasmon frequency of metals normally stands in the ultraviolet (UV) regime of the electromagnetic spectrum. Table 2.1 demonstrates the bulk plasmon wavelength of some important metals. [37]

Metal	Au	Ag	Cu
N (x 10^{28} m^{-3})	5.90	5.86	8.47
λ_p (nm)	138	138	115

Table 2.1: Free electron density and bulk plasmon wavelengths of common metals

2.3.2 Surface plasmons

Surface plasmons (SPs) are of interest to a wide range of scientists from physicists, chemists and materials scientists to biologists. Recently, a new interest in surface plasmons comes from progresses that allow metals to be structured and characterized on the nanometer scale.

This enables to control SP properties to reveal new aspects of their underlying science and to tailor them for specific applications. For example, Surface plasmons are already known for their potential in optics [38], magneto-optic data storage [39], microscopy [40] and solar cells [41], as well as being used to construct sensors. [42]

Surface plasmon polaritons (SPPs) are electromagnetic waves coupled to collective electron oscillations and propagating along the interface between a metal and dielectric media, exponentially decaying into both neighboring media. [43]

The resonant interaction between the surface charge oscillation and the electromagnetic field of the light constitutes the SP and promotes to its unique properties.

One of the most appealing aspects of surface plasmons is the way in which they help to concentrate and channel light using subwavelength structures. This could lead to miniaturized photonic circuits with length scales much smaller than those currently achieved. [44]
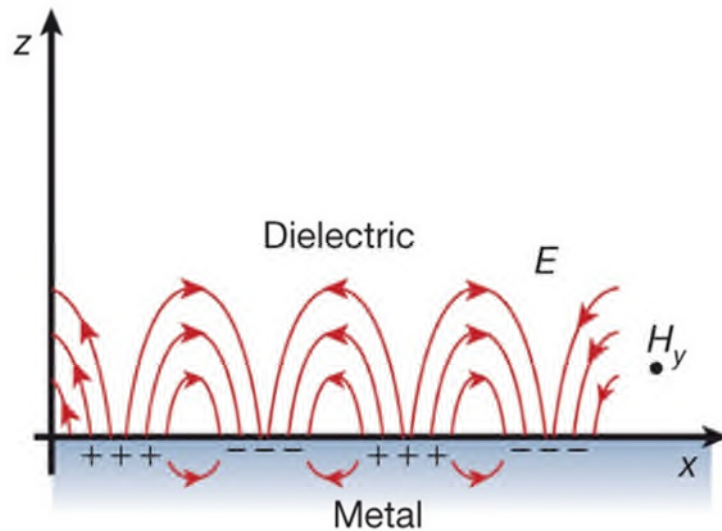
Figure 2.10: Surface plasmon polaritons (SPP) as a collective excitation at a metal–dielectric interface. The electromagnetic field (electric field, E, plotted in the z–x plane; magnetic field, H_y, sketched in the y direction) [45]

Whereas the confinement of light in a dielectric structure is ultimately constrained by the diffraction limit, plasmonic waveguides (figure 2.10) allow concentration of combined electronic and optical excitations (plasmon polaritons) to length scales far below the optical wavelength.

2.3.3 Maxwell's equations and wave propagation

The basic equations regulating the electromagnetic response, the macroscopic Maxwell equations, will be recalled before presenting an elementary description of the optical properties of metals. Further details on this topic can be found in textbooks like "Plasmonics: fundamentals and applications" from S. A. Maier. Maxwell equations are given by:

$$\nabla . D = \rho$$

$$\nabla . B = 0$$

$$\nabla \times E = -\frac{d}{dt} B$$

$$\nabla \times H = j + \frac{d}{dt} D$$

E, H, D and B represent the electric field, the magnetic field, the dielectric displacement and the magnetic flux density, respectively, ρ is the free charge density and j is the free current density. In optics it is usually assumed that the free charge and current are absent, i.e. $\rho = 0$ and j = 0.

18

Limiting to linear, isotropic and nonmagnetic media, these equations can define the constitutive relations:

$$D = \varepsilon_0 \varepsilon \ E$$

$$B = \mu_0 \mu \ H$$

Where ε_0 (~ 8.854 x 10^{-12} F/m) and μ_0 (~ 1.257x 10^{-6} H/m) are the permittivity and permeability of free space, respectively, ε and μ respectively represent the relative permittivity (or dielectric constant) and relative permeability of the medium (μ=1, for a nonmagnetic medium).

Assuming a time harmonic dependence for the electromagnetic (EM) field i.e. $e^{-i\omega t}$, then

$$\frac{d}{dt}e^{-i\omega t} = -i\omega e^{-i\omega t}$$

Where $\mathbf{i}$ is the imaginary unit and ω is the angular frequency. Then Maxwell's equations can be expanded in cartesian coordinates as follows:

$$\frac{dE_z}{dz} - \frac{dE_y}{dx} = i\omega\mu_0 H_x$$

$$\frac{dE_x}{dz} - \frac{dE_z}{dx} = i\omega\mu_0 H_y$$

$$\frac{dE_y}{dx} - \frac{dE_x}{dy} = i\omega\mu_0 H_z$$

$$\frac{dH_z}{dy} - \frac{dH_y}{dz} = i\omega\varepsilon_0\varepsilon E_x$$

$$\frac{dH_x}{dz} - \frac{dH_z}{dx} = -i\omega\varepsilon_0\varepsilon E_y$$

$$\frac{dH_y}{dx} - \frac{dH_x}{dy} = -i\omega\varepsilon_0\varepsilon E_z$$

19

SPP is a transverse magnetic (TM) polarized electromagnetic wave traveling along metal-dielectric interfaces. [36] The principle is demonstrated in figure 2.11 and it shows that the simplest geometry sustaining SPPs is a single, flat interface between a metal ($z < 0$, with a complex dielectric constant ε, in which the real part is negative) and a dielectric ($z > 0$, with a positive dielectric constant ε). Specifically, assuming that the SPPs wave propagates along the x-direction with a wavevector β, then d/dx=iβ , and that the structure is purely 2-dimensional, that is there is no spatial variation along the y-direction, then the Maxwell's equation can be simplified as follows:

$$\frac{dE_y}{dz} = -i\omega\mu_0 H_x$$

$$\frac{dE_x}{dz} - i\beta E_z = i\omega\mu_0 H_y$$

$$i\beta E_y = i\omega\mu_0 H_y$$

$$\frac{dH_y}{dz} = i\omega\varepsilon_0\varepsilon E_x$$

$$\frac{dH_x}{dz} - i\beta H_z = -i\omega\varepsilon_0\varepsilon E_y$$

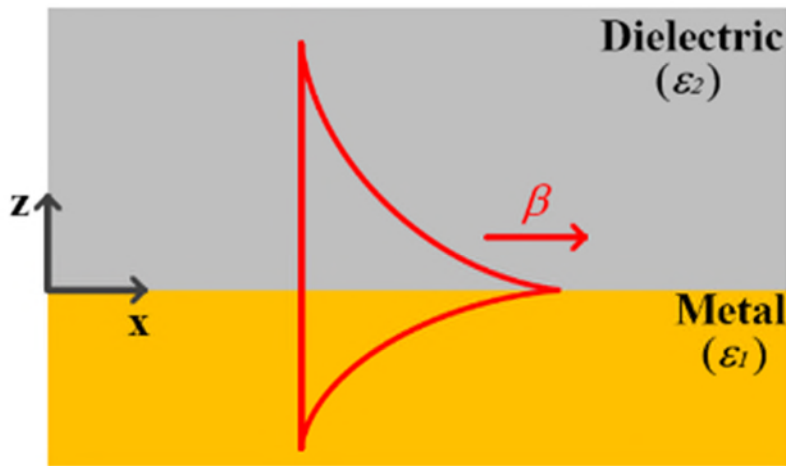$$i\beta H_y = -i\omega\varepsilon_0\varepsilon E_z$$

Figure 2.11: Schematic of SPPs spreading along a single metal-dielectric interface, ε is the dielectric constant and β the wavevector [46]

It can be easily revealed that the equation can be divided into two independent sets. For TM mode Maxwell´s equation is reduced to: (1) the transverse magnetic (TM) modes with only field components E_x, E_z and H_y being nonzero; and (2) the transverse electric (TE) modes, where only the field components H_x, Hz and E_y are nonzero.

For the TM mode the Maxwell´s equation is reduced to:

$$\frac{dE_x}{dz} - i\beta E_z = i\omega\mu_0 H_y$$

$$-\frac{i}{\omega\varepsilon_0\varepsilon}\frac{dH_y}{dz} = E_x$$

$$\frac{\beta}{\omega\varepsilon_0\varepsilon} H_y = E_z$$

The field components can be identified from the solutions of this equation. Using the equation set in both half spaces yields

$$H_y(z) = A_1 e^{i\beta x} e^{-k_2 z}$$

$$E_x(z) = \frac{iA_2 k_2}{\omega\varepsilon_2\varepsilon_0} e^{i\beta x} e^{-k_2 z}$$

$$E_z(z) = -\frac{A_2\beta}{\omega\varepsilon_2\varepsilon_0} e^{i\beta x} e^{-k_2 z}$$

In which

$$K_i{}^2 = \beta^2 - K_0{}^2 \varepsilon_i \qquad\qquad i = 1,2 \qquad\qquad (2.1)$$

The continuity of H_y and E_x at the boundary z= 0 results in:

$$A_1 = A_2 \qquad and \qquad K_1\varepsilon_2 = -K_2\varepsilon_1 \qquad (2.2)$$

By combining eq. (2.1) and eq. (2.2), the central result of this section, the dispersion relation of SPPs propagating at the interface between the two half spaces can be achieved:

$$\beta = k_0 \sqrt{\frac{\varepsilon_1 \varepsilon_2}{\varepsilon_1 + \varepsilon_2}}$$

The dispersion relation curve of the SPP is given in figure 2.12.

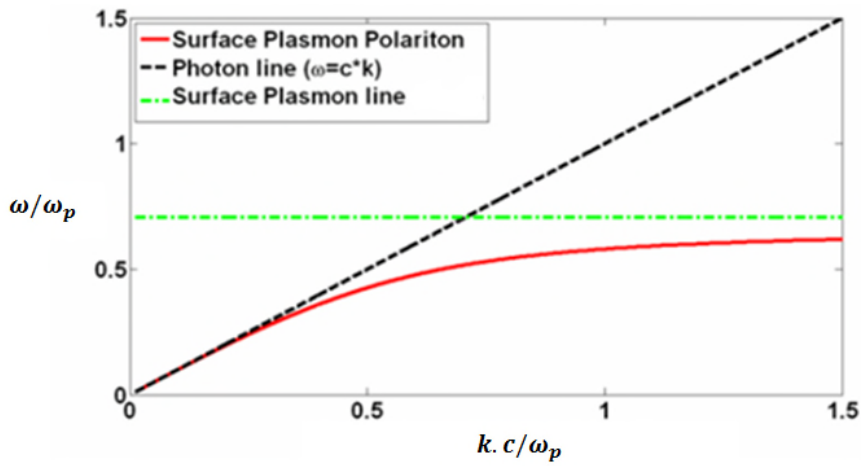Figure 2.12: Dispersion relation of free photon, surface plasmon and the surface plasmon polariton [47]

Where $k_0 = \omega/c$ is the wave vector of the propagating wave and c is the speed of light in vacuum. [44]

The frequency of the SPPs approaches the characteristic surface plasmon frequency and can be shown by inserting the free-electron dielectric function.

$$\omega_{sp} = \frac{\omega_p}{\sqrt{(1 + \varepsilon_2)}}$$

The motion of electrons results so unconventional because of the continuous collisions with the lattice. The plasma frequency is defined as the proper frequency of the collective motion of electrons in the way defined below:

$$\omega_p{}^2 = \frac{\sigma_0}{\varepsilon_0 \tau} = \frac{Ne^2}{\varepsilon_0 m}$$

σ_0 is showing the conductivity of the material and common meaning of the other mathematical symbols. The dielectric constant of the metal can be explained as a function to the plasma frequency that in first approximation results:

$$\varepsilon(\omega) = 1 - \frac{\omega_p{}^2}{\omega^2}$$

If it holds $\omega < \omega_p$, the dielectric constant is negative, therefore its square root is pure imaginary; this involves the reflection of the incident wave. In the contrary case, the square root of the dielectric constant is real and the incident wave can propagate in the medium with a small attenuation. [48]

2.4 Microresonator

Optical microcavities restrict light to small volumes by resonant recirculation. Devices based on optical microcavities are essential for a wide range of applications and studies. [49]

An important characteristic of a resonator is the quality of its optical confinement, which is defined by the quality factor (Q-factor). The quality factor of a cavity is defined as the ratio of the resonance frequency to the width of the resonance curve. While optical micro- and nanocavities made of dielectric or semiconducting materials represent large Q factors as well as small diffraction-limited cavity mode volumes, their metallic counter-parts have been optimized primarily for subwavelength-scale miniaturization and have given results well below the theoretically predicted performance limit – mainly in terms of cavity loss- set by ohmic loss in the metal.

The theory of light-dipole interaction in an optical cavity considers two physically distinct regimes, namely, the weak and strong coupling regimes. [50]

2.4.1 Purcell-effect

How the spontaneous emission rate can be modified by altering the local density of optical states around the emitter was described in 1946 by Edward Mills Purcell. This type of modification is known as the "Purcell effect". [51]

It has been revealed by Purcell that spontaneous emission is not only related to the emitter, but also depends on its environment. The case of an atom in a cavity with perfectly reflecting walls is a convincing example of this effect. If the dimensions of the cavity are smaller than half the wavelength of the atomic emission, no electromagnetic (EM) modes are supported by the system at a frequency ω, given by equation 2.3, and the atom will not decay.

$$\hbar\omega = E_2 - E_1 \qquad (2.3)$$

Where E_2 is the energy of the upper level and E_1 is the energy of the lower level (see figure 2.13).
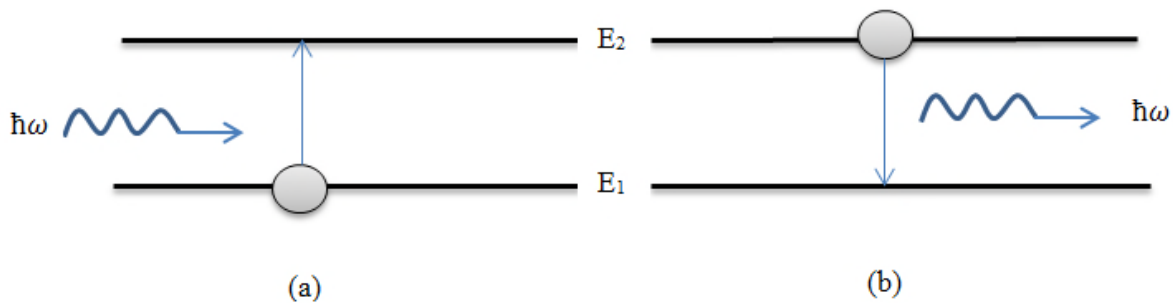

Figure 2.13: Schematic representation of the electronic transitions between two levels (of energies E_1 and E_2) of an emitter leading to absorption (a) and spontaneous emission (b) of photons.

This fact can signify that an emitter and its environment cannot be considered as two separate entities, as they interact and modify each other. Therefore this system must be considered as including both the emitter and the environment as a whole. [52]

According to the description above, the spontaneous emission of an isolated atom is due to an external perturbation and is forbidden in the first quantization picture. The situation is totally different if the EM field is also quantized (second quantization).

It could be assumed that the ground state, i.e., the absence of photons in the system, has an energy $E_{vac} = \frac{1}{2}\hbar\omega$, which is different from zero. This state is commonly known as the zero-point energy and originates from random fluctuations of the electric field known as the vacuum field. This can interact with an isolated emitter in an excited state and can make it decay to a lower energy level. The corresponding radiative transition rate can be calculated by fermi's golden rule:

$$\gamma = \frac{2\pi}{\hbar^2} |< f|\mu . E_{vac}|i >|^2 . \rho(\omega) \qquad (2.4)$$

24

Where γ is the transition decay rate from the initial (excited) state $|i>$ to the final state $<f|$, μ and E_{vac} are the electric dipole and vacuum-field operators evaluated at the emitter position, respectively, and ρ(ω) is the final photonic density of states.

Equation 2.4 enables to consider the spontaneous emission of an excited state as the stimulated emission due to the zero point fluctuations of the EM field. The density of final photonic states ρ(ω) is defined so that ρ(E)dE gives the number of final states which fall into the energy range E to E+dE, where E= ℏω. One can calculate ρ(ω) in vacuum by considering the EM modes within a cube of volume V, having

$$\rho(\omega) = V\,\rho_0 = V\,\frac{\omega^2}{\pi^2 c^3}$$

It should be taken into account that the arbitrary volume V serves as a computational tool and that it will disappear in the final result. The magnitude ρ_0 is the local density of states (LDOS) for vacuum, that is, the number of final states (modes) per unit volume with frequency ω. On the other hand, the transition matrix element in equation 2.4, averaged over all the possible directions, yields

$$|<f|\mu . E_{vac}|i>|^2 = \frac{1}{3}\mu_{if}^{\ 2} E_{vac}^{\ 2} \quad (2.5)$$

$\mu_{if}^{\ 2}$ being the square modulus of the electric dipole moment of the transition

$$\mu_{if} = -e <i|r|f>$$

where e is the electron charge and r is the position operator. The vacuum electric field can be obtained by equating the EM energy in a volume V with the zero point energy

$$\int \varepsilon_0\, E_{vac}^{\ 2}\, dV = \frac{\hbar\omega}{2}$$

which implies

$$E_{vac} = \sqrt{\frac{\hbar\omega}{2\varepsilon_0 V}} \qquad (2.6)$$

The decay rate of an isolated emitter is defined as:

$$\gamma_{free} = \frac{1}{\tau_{free}} = \frac{\mu_{if}^2 \omega^3}{3\pi\hbar c^3 \varepsilon_0} \qquad (2.7)$$

where τ_{free} is the radiative lifetime. Remarkably equation 2.7 has exactly the same form of the classical expression for the radiative damping of an electric dipole in vacuum. [53]

2.4.2 Weak coupling

The contribution of emitter and environment to the decay rate, γ, split into two parts in equation 2.4. The matrix element considers the quantum mechanical properties of the emitter, while the density of states, $\rho(\omega)$, reflects the influence of the environment. A similar situation occurs when the emitter is placed in a cavity and their interaction is said to be weak. [52]

Only specific EM modes will be supported depending on the characteristics of the cavity. Dimensions, shape, and composition are such of these characteristics. This means that the cavity will only allow certain final states into which photons can decay. As an example, if an emitter is placed close to a metal nanoparticle (NP), the final density of states will have a peaked maximum at the plasmon resonance wavelength, as it provides a new and strong decay channel for the emitter.

If a cavity be considered that supports only one mode of frequency, ω_c, the density of states, $\rho(\omega)$, can be described by the Lorentzian function:

$$\rho(\omega) = \frac{2}{\pi} \frac{\Delta\omega}{4(\omega - \omega_c)^2 + \Delta\omega^2}$$

Characterized by the quality factor, $Q = \omega_c/\Delta\omega$, of the cavity, where $\Delta\omega$ is the width of the LDOS maximum at $\omega = \omega_c$. [54]

If an emitter located in the cavity has an electronic transition at $\omega_0 = \omega_c$, the cavity is said to be tuned to the emission frequency, and the density of states at $\omega = \omega_0$ is

$$\rho(\omega_0) = \frac{2Q}{\pi\omega_0} \qquad (2.8)$$

The transition matrix elements of the system and those of the free emitter can relate together; using equations 2.5 and 2.6:

$$|< f|\mu \cdot E_{vac}|i >|^2 = \beta^2 \frac{\hbar\omega\mu_{if}^2}{2\varepsilon_0 V}$$

where V is the cavity volume and β is a factor that takes into account the dipole moment orientation. [55] When it is randomly oriented, $\beta^2 = 1/3$.

The decay rate of an emitter placed within a plasmonic cavity can then be calculated with use of equations 2.5 and 2.8:

$$\gamma_{cav} = \beta^2 \frac{\mu_{if}^2}{\varepsilon_0 \hbar} \frac{Q}{V} \quad (2.9)$$

The Purcell factor is the emission rate enhancement of a spontaneous emitter inside a cavity or resonator. For an emitter parallel to the field direction ($\beta^2 = 1$) and with use of equations 2.7 and 2.9: [56]

$$F_p = \frac{\gamma_{cav}}{\gamma_{free}} = \frac{\tau_{free}}{\tau_{cav}} = \frac{3}{4\pi^2} Q \left(\frac{\lambda^3}{Vn^3}\right) \quad (2.10)$$

F_P is known as the Purcell factor. $c/\omega = n(2\pi/\lambda)$, where n is the cavity refractive index. F_P describes how the decay rate of the emitter is modified by the presence of the cavity. If $F_P > 1$, the spontaneous decay rate is enhanced; in other ways the cavity inhibits the emission. [52]

As formulated in equation 2.10, F_P is proportional to the quality factor Q, of the plasmonic resonance and inversely proportional to the mode volume. As plasmonic structures concentrate EM fields into subwavelength volumes, they are suitable to manipulate the decay rate of emitters despite the fact that such structures do not have resonances with very high quality factors ($Q \approx 10$-100 or $3/4\pi^2Q \approx 1$-10).

Nevertheless, the highly reduced mode volume of localized surface plasmon resonances (LSPRs) enables a strong enhancement of the decay rate of emitters, given by the factor $\lambda^3/(Vn^3)$ in equation 2.10. The diversity of the optical cavities with an ultra-small size has proven to be promising candidates for developing an all-optical switch, which are capable of being integrated on a chip. Recent advances in nanofabrication processes have made it possible to perceive an ultrahigh Q of more than 10^6 while keeping a small mode volume comparable to $(\lambda/n)^3$. [57]

2.4.3 Strong coupling

The quality factor of a cavity mode is conjoined to the time, $\tau_{cav} = 1/\gamma_{cav}$, that a photon spends in the cavity or, in the matter of a plasmonic resonance, to the lifetime of the localized surface plasmon resonance (LSPR). This provides with a strategy to quantify the strength of the interaction between the cavity and the emitter. If the lifetime of the LSPR is very short compared to the reversal of the spontaneous decay rate of the isolated emitter, it is in the limit of weak coupling. In this case, resonant photons are retained for a short time and interact very little with the emitter.

A different scenario occurs when the lifetime of the plasmonic resonance is significantly longer than the spontaneous emission lifetime in free space. [52]

For the purpose of describing the strong interaction between cavity and emitter, their interaction probability must be introduced. Strong and weak regimes of interaction can be differentiated from each other via the basis of the atom-field coupling constant κ, which is defined as the interaction energy. [54]

$$\hbar k = |\mu_{if} . E_{vac}|$$

And subsequently after inserting E_{vac}:

$$k = \frac{\mu_{if}}{\hbar} \sqrt{\frac{\hbar \omega}{2 \varepsilon_0 V}} \qquad (2.11)$$

Strong coupling satisfies the condition $\kappa \gg \gamma_{cav}$. In this regime, photons remain in the cavity for an extended period of time and are absorbed and re-emitted multiple times before being radiated out of the structure. This leads to a strong coupling between cavity and emitter, which must be considered as a unique system instead of two separate entities. Importantly, an accurate description of such a system can only be obtained through a full quantum electrodynamic treatment.

Equation 2.11 demonstrates the advantage of using the minor volumes of LSPR in the strong coupling regime. In the strong-coupling regime a reversible exchange of energy, known as Rabi oscillations, exists between the emitter and the cavity field for an emitter coupled to a metal nanoparticle. [54] The strong coupling between single emitters and the LSPRs of metallic nanostructures represents an exciting frontier in plasmonics, in particular when their use for quantum optics applications is considered. The subwavelength confinement of guided plasmon modes in nanowires leads to a strong coupling between these EM modes and nearby emitters in the optical domain. [52]

3. Experimental

This chapter describes the practical experiments of this study giving a short introduction to common processes in the cleanroom, followed by a detailed description of sample fabrication and structuring processes. Further a short description of the used laser setup for PL spectroscopy is shown. Finally the MEMS straining device and the fabrication process are described.

3.1 Silicon nanowire synthesis and device fabrication

The nanowires used for this study, were thankfully synthesized by Dipl.-Ing. Dr. Stefan Wagesreither in a low pressure chemical vapor deposition LPCVD system, utilizing the VLS mechanism with silane as precursor gas and gold (Au) as catalyst.

A silicon dice is cleaned by acetone and isopropanol using sonification, dipped in buffered hydrofluoric acid (BHF) for 5 s to remove the native SiO_2 layer and subsequently rinsed with deionized water. 10 μl of the Au colloid solution solved in deionized (DI) water with a mixing ratio of 1:5 is dropped on the silicon dice in order to deposit the catalytic gold colloids with diameter of 80 nm. The sample is dried on a hot plate, once again dipped in BHF for 10s and afterwards rinsed in DI water. The second BHF dip is required to remove the oxide from the gold collide surface originating by silicon diffusion through the gold. [58]

Afterwards, the sample is immediately introduced into the LPCVD reactor and in order to prevent re-oxidation of the silicon, the tube is evacuated to a pressure <0.05 mbar. After evacuation the tube is purged with 70 sccm Helium (He) and the oven is heated up with a ramp of 60 K/min to the final growth temperature of 793 K. The pressure is regulated to 3 mbar with the manual throttle during the heating phase. He flow is stopped at the time that the growth temperature is reached and the process gases, 10 sccm H_2 and 100 sccm diluted SiH_4 (2% SiH_4 in He) are started.

During the whole growth duration the temperature was kept constant. After completion of a 45 min growth duration the gas flows are stopped and during the cool down of the furnace, the tube is purged with He.

The sample is finally removed from the LPCVD reactor at a temperature of approximately 573 K. A typical growth rate of silicon nanowire under the given growth conditions is suggested to be about 110 nm/min. Due to this reason, for a growth duration of 45 min, the nanowires have a length of about 5μm. [21]

The processing steps for formation of plasmonic nanowire device are shown in figure 3.1. The silicon nanowires were growth on Si (111) substrates via a gold-catalyzed VLS growth, figure 3.1.a. Figure 3.1.b shows, that the catalyst was removed by wet chemical etching after growth, to avoid gold contaminations. The nanowires were immersed by sonication in isopropanol. Nanowires were subsequently deposited on glass substrates by drop casting (figure 3.1.c).
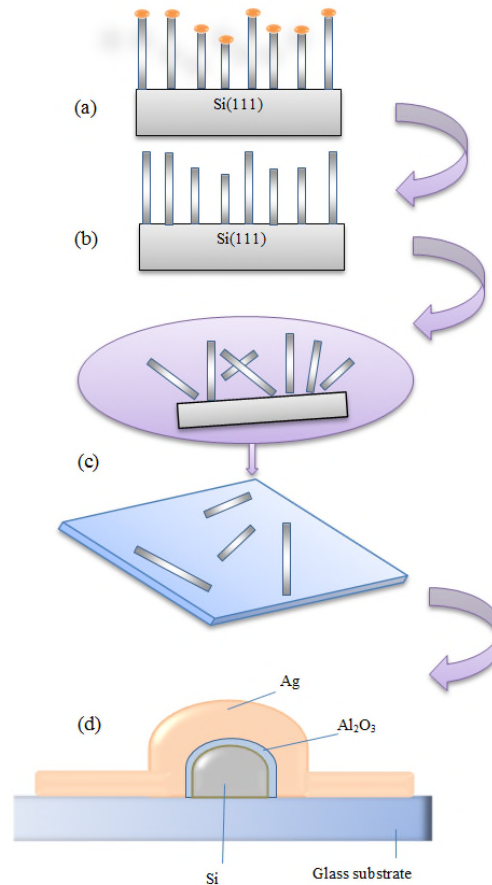
Figure 3.1: Formation of plasmonic nanowire device is shown in sequential sample processing steps: (a) Gold-catalyzed VLS nanowire growth, (b) gold removal by wet etching with aqua regia, (c) Deposition of nanowires on a glass substrate by immersion in isopropanol via sonification (d) Fabrication of an **Ω**-shaped plasmonic nanocavity-coupled silicon nanowire device by depositing a Al_2O_3 interlayer, followed by a silver Ω-shaped cavity to support surface plasmon polariton modes

Afterwards a plasmonic nanocavity was fabricated on individual silicon nanowires. As described, the nanowires were dispersed in isopropyl alcohol via an about 5 second sonification step and drop cast on 130 µm thick glass coverslip slides. A 3 nm Al_2O_3 interlayer was deposited via atomic layer deposition (ALD) and served to prevent exciton quenching at the metal surface. For the thickness of oxide layer about 3 nm, 30 cycles of each 0.1 nm will be used, deposited by ALD. This was followed by a 100 nm of silver (Ag) layer deposited via electron beam evaporation (Leybold with rate of 0.05 nm/s). To avoid inclusion of impurities, the pressure during the evaporation process is less than 10^{-6} mbar. The resulting structure is an Ω-shaped metal nanocavity (figure 3.1.d) to support SPP modes.

It is now possible to excite SPPs and achieve strong light–matter interactions inside the NW structures by combining wavelength scale or subwavelength scale nanowires and metallic structures.

A metal frame was constructed for the sample to perform the PL measurements. Therefore the glass substrate is placed inverted on a metal frame. Figure 3.2 shows a schematic construction of the sample for the PL measurement.
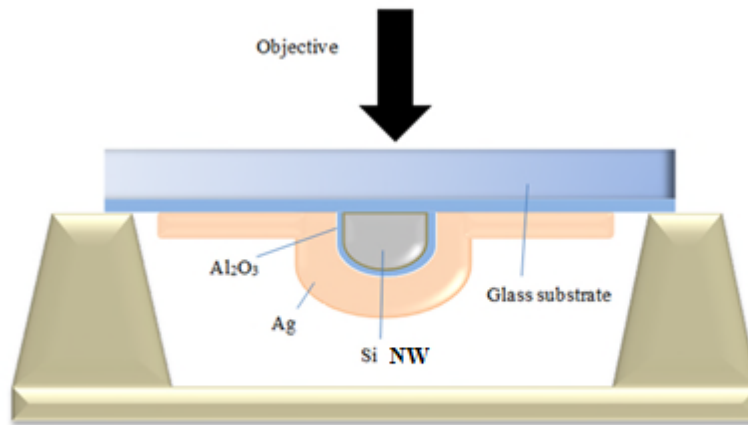
Figure 3.2: schematic setup for measurement. An Ω -shaped plasmonic nanocavity-coupled silicon nanowire device by depositing a Al_2O_3 interlayer, followed by a silver Ω-shaped cavity is placed inverted on a metal frame for the PL measurements

3.2 Used equipment

3.2.1 Atomic layer deposition

A particular type of chemical vapor deposition process for thin film oxides is called ALD, which applies layer by layer self-limiting or sequentially self-terminating films on atom level.

ALD process is utilizing several precursor gases that act as reactants for a chemical surface reaction. The function of vacuum is used to separate the reactions of the precursor gases at the surface and the inlet of two precursor gases into the process chamber is altered in a cyclic way. This kind of chemical surface reaction is a self-limiting reaction; which means that every cycle results in the formation of a mono-layer. For this reason, the layer thickness can be precisely controlled at an atom in level. In this study, the deposition was performed by using a Cambridge NanoTech Savannah S100 ALD system. Al_2O_3 was used as interlayer oxide. Trimethylaluminum and vaporized water were used as precursor gases. The total reaction of the process is:

$$2Al(CH_3)_3 + 3H_2O \rightarrow Al_2O_3 + 6CH_4$$
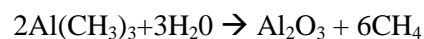
Thus, producing the Al_2O_3 film and by-product methane gas is affected; the CH_4 does not react with any of the other species in the deposition process and, so, can be considered inactive. [59]

3.2.2 Rapid thermal annealing

A thermal oxidation in a rapid thermal annealing (RTA) oven was used in order to obtain a protective SiO_2 layer on nanowire. There is a high advantage of RTA compare to the standard annealing process; in fact the possible steep temperature profiles. It should be mentioned that in the case of silicon, it is possible to rebuild a crystal structure by the means of annealing and also to oxidize silicon creating well defined oxide layers. The crucial parameters of this part of experiment are principally the temperature and processing time. Utilization of different gases to flood the chamber is possible but very often, inert gases like nitrogen or argon are used; however oxygen and other gases that have a direct effect on the sample may also be used.

3.2.3 Electron-beam evaporation

A nanowire covered by 100 nm Ag layer was used in order to support the surface plasma polarization. For the Ag layer deposition a Leybold e-beam evaporation system was applied. Electron-beam assisted evaporation (EBAE) is a type of physical vapor deposition (PVD). In this process, a metallic target is heated above the evaporation temperature by using an electron-beam. Certain materials can be deposited on a substrate by initially transforming them from solid to the vapor state in a vacuum and then letting them condense onto the substrate surface.

A sample which was located within the line-of-sight and opposed to the target prepared a suitable condition for the atoms to precipitate into solid form. Thus, the sample was mounted upside down in a high vacuum chamber with a pressure of about 10^{-7} mbar. The deposition rates were deemed to be quite low and could be controlled by regulating the cathode current appropriately.

3.2.4 Sputter deposition

The deposition of different types of metals and even high melting insulators is achieved by using the process of sputtering. After a particular pressure is reached the chamber is flooded with argon (Ar) ions to enable the ignition of a plasma between the sample and the target material. The target is bombarded by argon ions due to the electrical field. Thereby, target atoms are ejected and deposited on the sample. For this purpose, the Ardenne LS 320 S sputter system was used. Sputter deposition (SD) provides conform deposition at high rates.

3.3 Spectroscopy

In this part of the study, a Witec alpha300 confocal microscope system (High-Resolution Confocal Raman Microscopy) in backscattering geometry at ambient laboratory conditions was applied for performing Raman spectroscopy. All Raman and PL measurements were conducted using this microscope system. The main components of the system are shown in figure 3.3.
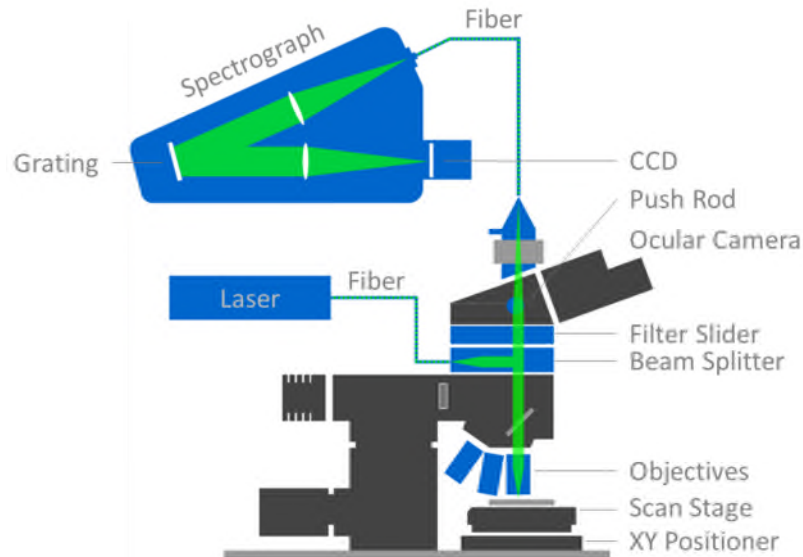

Figure 3.3: The construction components of Witec alpha300 confocal Raman imaging microscope [60]

The samples were located in the position below the microscope on a 3-axis piezo-actuated stage. As pulsed excitation source a frequency-doubled Neodym-doped Yttrium-Aluminium-Granat-Laser (Nd:YAG Laser) with continuous-wave emission at $\lambda = 532$ nm was applied. This type of laser as one of the most common types of laser is optically pumped using a flashtube or laser diodes. Neodymium ions in different forms of ionic crystals act as a laser gain medium emitting the light from a particular atomic transition in the neodymium ion, after being "pumped" into excitation from an external source. For PL spectroscopy was used a multimode fiber as waveguide from alpha300 to spectrograph.

The beam splitter acts as a light deflector towards the sample. The collimated beam needs to be focused in an objective before impinging on the sample. The back scattered light once more traverses objective and beam splitter and is guided in the direction of the fiber coupling unit on top of the device. The Rayleigh scattered light attenuates strongly by a filter, which is positioned between the beam splitter and the fiber coupling unit. The fiber guides the light into the spectrometer, where it is dispersed with the aid of a grating. The fiber acts as a pinhole. Finally the light reaches a charge-coupled device (CCD) camera. This camera digitizes the output spectrum of the scattered light.

The beam path can be changed for the usage of the digital microscope (viewing mode) by repositioning push rod and filter slider. In fact, it is clear that the internal light source of the microscope needs to be turned on in order to illuminate the sample surface. In this mode, the user is able to navigate across the sample surface with assistance of the XY positioner. The scan stage allows

highly resolved automated scanning in the measurement mode, according to a previously defined pattern.

The system needed to be adjusted, before any spectroscopic measurements being carried out. The adjustment of the setup basically works equally for both measurement modes (Raman, PL); however, a new calibration would be necessary prior to any type of changes in the setup of the system.

As the first step, the standard components (beam splitter, filter, fiber, and spectroscope), which are required for a proper measurement should be assembled properly to the system. Furthermore, the focus plane of the microscope and the laser needed to be matched against each other. Therefor the microscope was focused on the sample surface, which was set at low laser power. The laser spot was focused onto the same surface employing the collimator screw on the back side of the beam splitter. Next, the system was changed into measurement mode to precisely adjust the coupling into the fiber. For this purpose, the desired grating within the spectrograph was selected and a real-time oscilloscope with an integration time of 0.1 s was started in the measurement software. The fiber coupling unit at the top of the microscope exhibits two screws to align the horizontal position of the fiber. By these means the fiber was adjusted in a way that a maximum spectral intensity could be achieved. The laser power impinging on the sample surface was determined with the aim of a Thorlabs PM100D power meter connected to an S121C Si photodiode detector. Silicon photodiode arrays consist of multiple elements, which are built in a linear arrangement at an equal spacing and they are used in a broad range of applications (e.g. laser beam position detection and spectrophotometry). [33, 60]

The measurements of this work were exclusively performed in a dark room and under ambient conditions. The preferences and the details of the setup configurations used for spectroscopy are described in the following part of the study.

3.3.1 Raman measurements

The Raman process contains the interaction of incoming electromagnetic radiation with the vibrational states of a material. The center position of the grating was set at 614 rel cm^{-1} for all Raman spectra. The spectral width using the grating with 1800 grooves per millimeter (g/mm) is > 1150 cm^{-1} resulting in a pixel resolution of < 0.9 cm^{-1}. [51]

By altering the integration time, the intensity of the gathered spectra could be adapted properly. To increase the signal to noise (S/N) ratio, the software also provides the possibility to do several accumulations of the same spectrum and calculate an averaged spectrum. Typical values for integration time were 15 or 20 s and the number of accumulations was normally 2. To avoid laser heating of the sample and thus a temperature dependent shift of the Raman spectra, the laser power on the sample surface was kept low. In most cases, laser powers around 93 μW were adjusted for Raman measurements.

For Raman spectroscopy, the system configuration was as follows:

- Nikon EPI E-Plan 100x objective (NA = 0.9, WD = 0.23 mm)

- Dichroic beam splitter

- Semrock 532 nm RazorEdge long-pass edge filter

- Multi-mode fiber with a core diameter of 100 μm

- WITec UHTS300 spectrograph with 1800 g/mm grating

- Andor iDus DV401A-BV CCD detector (1024 × 127 pixel)

3.3.2 Photoluminescence measurements

Photoluminescence spectroscopy was also performed likewise with the same detector as for Raman investigation. To cover a wider spectral range, the grating with 600 g/mm was chosen, resulting in a spectral width of approximately 130 nm. [60]

Since vignetting of the lenses restricts exact measurements just around the spectral center of the grating, an overlap of the spectra from two consecutive measurements was adjusted. The measurement was usually started at a center wavelength of 1006 nm which was successive reduced by 66 nm down to 610 nm, resulting in 7 overlapping spectra. The envelope of thus obtained spectra was extracted and corrected by the means of a data analysis software. An integration time during the measurement was usually 15 to 20 s. A laser power of approximately $240 - 250$ μW was adjusted for PL measurements.

The system configuration for photoluminescence spectroscopy was:

- Nikon EPI E-Plan 100x objective (NA = 0.9, WD = 0.23 mm)

- Holographic beam splitter

- Semrock 532 nm StopLine single-notch filter

- Multi-mode fiber with a core diameter of 100 μm or multi-mode fiber with a core diameter of 910 μm

- WITec UHTS300 spectrograph with 600 g/mm grating

- Andor iDus DV401A-BV CCD detector (1024 × 127 pixel)

3.4 Design of the electrostatic-actuated-straining-device

This chapter describes the MEMS straining device. The device used in this work, was fabricated by Dipl. Ing. Dr. Stefan Wagesreither. The MEMS device consists of three basic parts (figure 3.4). The electrostatic comb drive actuator is composed of sections of the actuator and the stage part. The silicon nanowire is monolithically integrated between stage part and the fixed specimen part. Each part is connected with a macroscopic silicon pad suitable for wire bonding. The comb drive actuator is designed with two rows of comb drive elements to increase the total number of elements and therefore the attainable actuator force. The section of the stage part which is part of the actuator is suspended to provide the movability of the actuator combs.

Due to an applied voltage on the actuator part, the suspended stage part can be attracted toward the actuator part and in the same way; it will be pulled apart from the specimen part. Hence the nanowire integrated between stage and specimen part will be uniaxial tensile strained. For the fabrication of silicon nanowire device coupled with an Ω-shaped cavity a hole has been made by reactive ion etching (RIE) on the back of the device. The Ag layer was deposited through this hole.
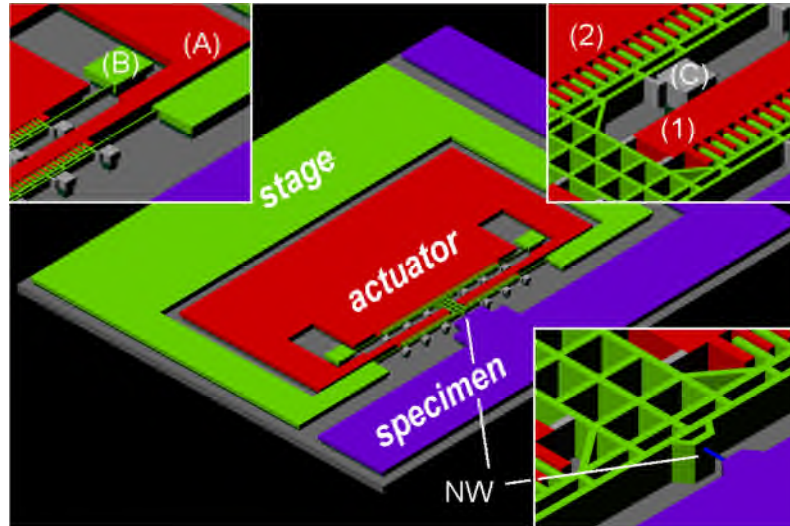

Figure 3.4: Schematic of the EASD with the red colored actuator part, the green colored stage part and the purple colored specimen part. The inset shows a magnification of the gap between stage and specimen part with the monolithically integrated silicon nanowire (blue). [61]

Hydro-adhesive forces can lead to a sticking of the suspended EASD parts on the underlying substrate. Especially wet chemical processes during device fabrication and nanowire integration involve risk for such sticking. Therefore the suspended stage part is supported by silicon beams connected to the actuator part and isolated pads (C) at sixteen positions. These beams prevent the suspended stage part from sticking on the bulk substrate to during the whole nanowire integration. They are finally removed by focused ion beam (FIB) cutting. [61]

4. Results and discussion

This chapter is focused on the experimental results, which were obtained throughout the course of this thesis. The focus of this work was on the specific properties of plasmon nanocavities to enhance PL of silicon nanowires. To understand the interaction of silicon phonon modes and nanocavity plasmon resonances leading to efficient light emission, PL measurements were carried out. This work is based on the published study R. Agarwal et. al [5], which shows a new method to achieve bright visible light emission in 'bulk-sized' silicon coupled with plasmon nanocavities at room temperature, from non-thermalized carrier recombination. In the first part PL measurements of a plasmonic silicon nanowire device with an Ω-shaped Ag cavity are presented. Afterward the PL measurements of the silicon nanowire with cavity in a MEMS device are presented and finally the correlation between PL-peak shift and strain is explained.

4.1 Photoluminescence measurements

PL measurements were executed with the setup described in chapter 3.3. Room-temperature µ-PL measurements were performed on individual nanowire devices with a Nd:YAG laser excitation source. For PL measurements, a laser power of approximately 240-250 µW was adjusted. The nanowire embedded in an Ω-shaped metal cavity was excited and measured through the substrate. Bright visible light emission was observed from individual plasmonic silicon nanowires of different thicknesses.

4.1.1 PL analysis of a plasmonic silicon nanowire device with an Ω-shaped silver cavity

Figure 4.1 shows a SEM image of a silicon nanowire coated with an Al_2O_3-layer and silver and diameter with $d_{min} = 63$ nm at tip to $d_{max} = 95$ nm at base. After a 3 nm Al_2O_3-layer a silver film (100 nm) was deposited on the silicon nanowires using electron beam evaporation techniques. Silver was used due to its strong plasmonic resonances as well as relatively low dissipation in the visible frequency range.

At least when the nanowire was illuminated, broad hot luminescence spectra could be measured from the excitation region.
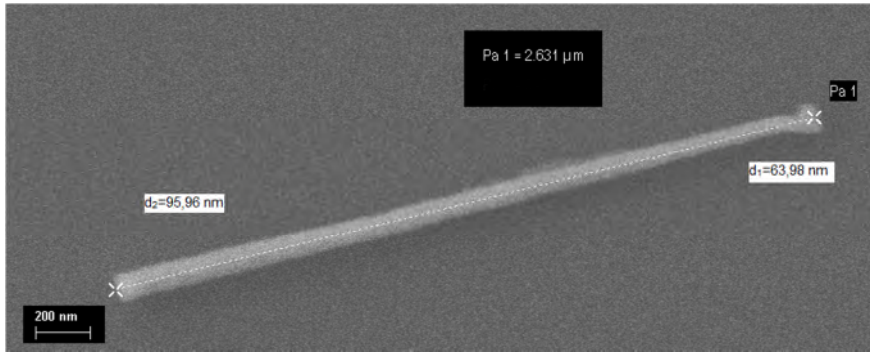
Figure 4.1: Scanning electron microscope (SEM) image of the fabricated nanowire

The blue curve in figure 4.2 shows a spectrum of silicon nanowire without a plasmonic cavity. There are no observable photons counts as expected from bulk silicon. On the other hand, the spectrum of the nanowire coupled with the plasmonic Ω-shaped silver cavity shows broad luminescence over the visible spectrum (red curve). The resulting PL points a broad envelope, which starts just short-term after the laser line. This advises that the observed emission is indeed hot-carrier photoluminescence.
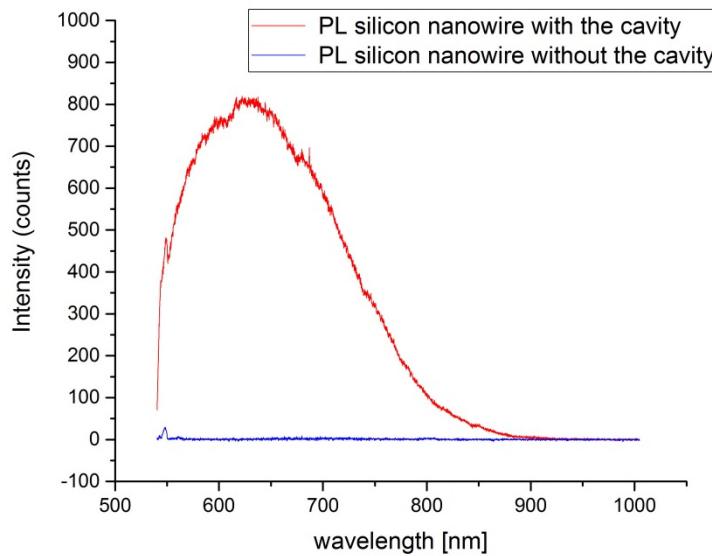

Figure 4.2: PL spectra from a silicon nanowire device coupled with a 3 nm Al_2O_3 and 100 nm **Ω**-shaped Ag cavity (red) and silicon nanowire without cavity (blue)

In a hot photoluminescence mechanism, excited charge carriers may undergo two competing processes (figure 4.3), thermalization to the minimum of the conduction band via non-radiative phonon scattering and scattering back into the light line.
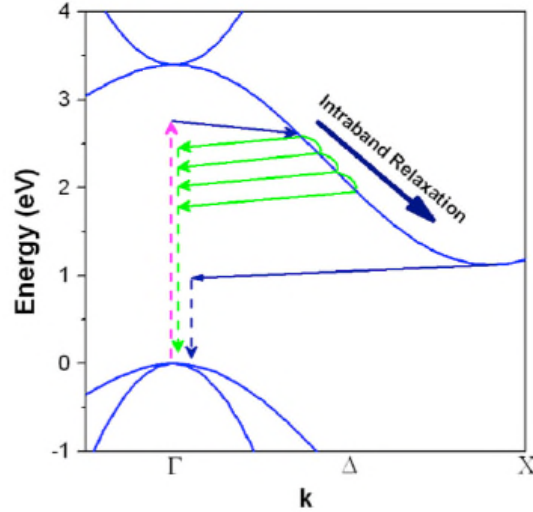
Figure 4.3: Schematic of the electronic band diagram of bulk crystalline silicon, illustrating phonon-assisted hot luminescence processes (green arrows) before thermalization of the carriers to the minimum of the conduction band near the X-point (blue arrows) [5]

Radiative recombination from high energy states above the conduction band minimum is conceivable if the spontaneous emission lifetime in range of ns becomes comparable to that of the non-radiative recombination process (<1 ps), and if there is a sufficient source of slightly available phonons to join in the scattering process. [62]

To study the nanocavity induced Purcell enhancement and the corresponding electromagnetic field distribution, numerical simulations for the Ω-shaped devices were needed, which was not possible in this work.

According to Agarwal et al. [5], for the highly confined plasmonic cavity modes, the quality factor was estimated to be $\sim$30, together with an ultrasmall mode volume of $\lambda^3/10^4$ (λ is the free-space wavelength), giving rise to a large radiative rate enhancement (Purcell factor of 1×10^3).

After the Ag deposition, the sample was measured within a few hours. The reason is that the PL spectra of silicon nanowire device coupled with a Ω-shaped cavity become weaker over time. A comparison between two measurements immediately after Ag deposition and 3 weeks later is shown in figure 4.4. Ag layer oxidizes in the room temperature and the oxidation of the Ag layer surface probably prevents the effect of plasmons and decreases the PL peaks.
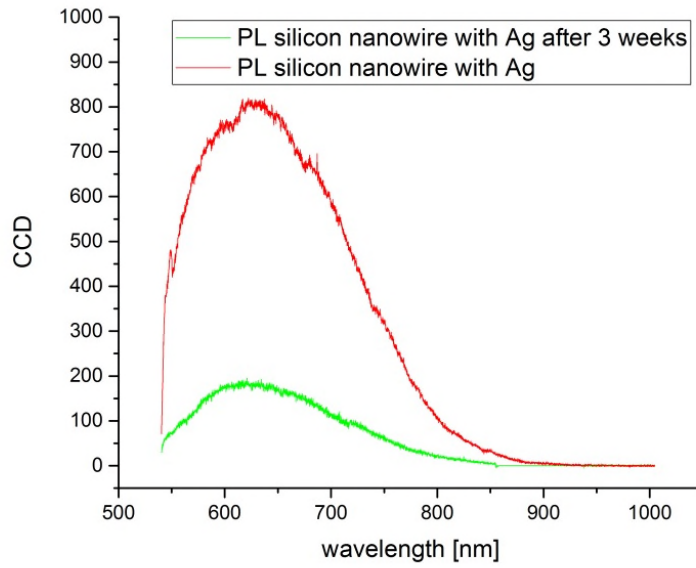
Figure 4.4: PL spectra from a silicon nanowire device coupled with an **Ω**- shaped Ag cavity (3 nm Al$_2$O$_3$ and 100 nm Ag). Comparison PL spectrum immediately after Ag deposition (red) and 3 weeks after Ag deposition (green)

4.1.2 Influence of the oxide layer on the photoluminescence spectrum

In this experiment an oxide layer is used as an insulating interlayer to separate the active material from the metal of the Ω-shaped cavity. This layer ensures that the non-radiative recombination of charge carriers at the metal surface is inhibited. Two different oxide layers, namely SiO$_2$ and Al$_2$O$_3$, are deposited on silicon nanowires by two different methods; ALD and thermal oxidation in a RTA oven (see chapter 3.2).

PL Measurements from silicon nanowires with two diverse oxides SiO$_2$ and Al$_2$O$_3$ are shown in the following plot, which will be denoted as NW1 and NW2 for reasons of simplicity.

Physical dimensions of the two nanowires devices are given in table 4.1.

denotation	Length [μm]	Min. diameter [nm]	Max. diameter [nm]	Oxide	Thickness [nm]
NW1	3.9	87.89	140.6	SiO$_2$	3
NW2	2.23	88.8	133	Al$_2$O$_3$	3

Table 4.1: Physical dimensions of the silicon nanowires used for PL-measurements

Figure 4.5 presents broad hot luminescence spectra with high counts obtained from two silicon nanowires coupled with the same Ω-shaped cavity material, 100 nm Ag, but different oxide.
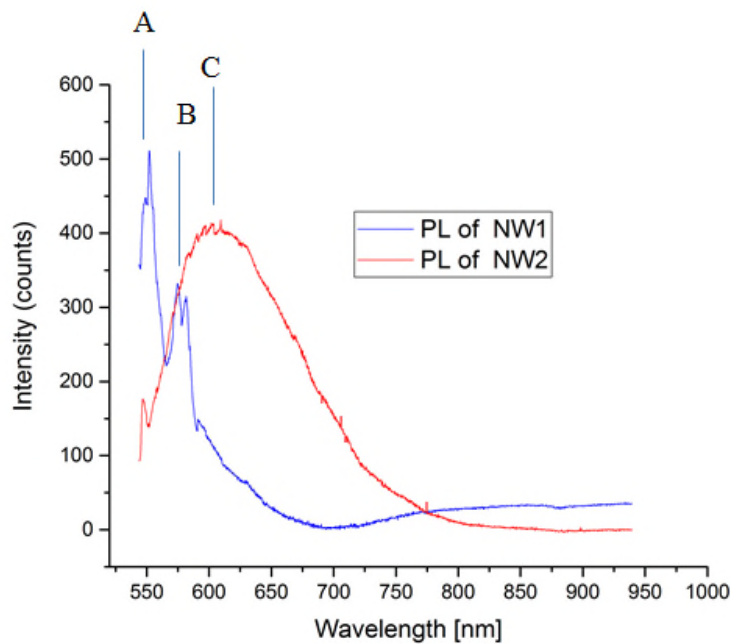

Figure 4.5: PL spectra from plasmonic nanowires devices with SiO_2 and Al_2O_3 as interlayer. The blue curve shows a PL spectrum of Ω-cavity silicon nanowire with a diameter of ~87 nm to ~140 nm and 3 nm SiO_2 followed by a 100 nm Ag Ω -shaped cavity. The red curve belongs to a silicon nanowire with a diameter of ~88 nm to ~133 nm and 3 nm Al_2O_3 followed by a 100 nm Ag Ω -shaped cavity

The resulting PL spectrum of Ω-cavity silicon nanowire with SiO_2 as interlayer has a sharp peaks in comparison to broad peak of a Ω-cavity silicon nanowire with Al_2O_3 as oxide interlayer. The first peaks of PL spectra (A) of the both devices at approximately 543 nm–549 nm correspond to the Raman peaks of silicon at 542 nm. The second peak (B) of silicon cavity with SiO_2 at λ = 579 nm is the resulting PL spectrum of Ω-cavity silicon nanowire. The broad-band PL (C) of the device with Al_2O_3 oxide was obtained with a center wavelength of approximately 605 nm. The oxide interlayer served to prevent exciton quenching at the metal surface while further passivating the silicon nanowire. Since the thickness of oxide in both nanowires is equal, it can be assumed that the deposited Al_2O_3 has a better effect on PL by ALD.

4.1.3 Influence of the nanowire diameter on the photoluminescence spectrum

To investigate this case, two silicon nanowires with different diameters were studied. Figure 4.6 shows the PL measurements of two nanowires devices. According to Agarwal et al., the spectral position of PL is sensitively dependent on nanowire diameter. [5]

41

To test the effect of cavity size on hot luminescence, divers plasmonically-coupled nanowires were measured (table 4.2). Figure 4.6 shows the PL measurements of two nanowires.

denotation	Min. diameter [nm]	Max. diameter [nm]	Oxide	Metal
NW1	125	157	5 nm Al_2O_3	100 nm Ag
NW2	90	115	5 nm Al_2O_3	100 nm Ag

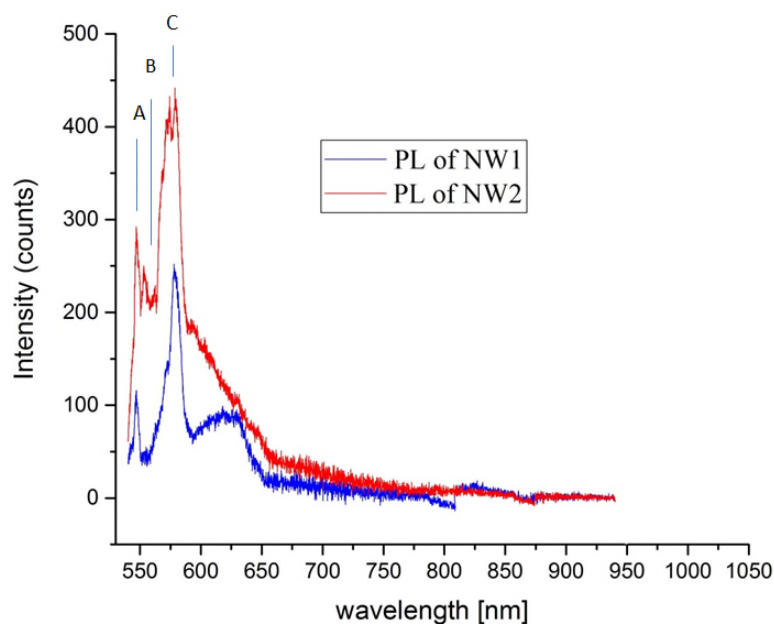Table 4.2: Physical dimensions of the silicon nanowires used for PL measurements

Figure 4.6: PL spectra from the NW1 (blur curve): silicon nanowire device with a diameter of 125 nm coupled with an Ω-shaped cavity (5 nm Al_2O_3 and 100 nm silver film), PL spectra from the NW2 (red curve): silicon nanowire device with an diameter of 90 nm coupled with an Ω-shaped cavity (also 5 nm Al_2O_3 and 100 nm silver film)

Figure 4.6 shows a clear peak structure overlapped on the hot luminescence background. As well as the previous measurement, the PL shows a peak at about 545 nm (peak A), which corresponds to the silicon Raman peak. In NW2 (d = 90 nm) peak B still shows a PL spectrum at 555 nm, which indicates a better plasmonic resonator in thinner silicon nanowire. High PL spectra can be seen at the wavelengths of 575 nm and 580 nm (peak C). At this point, the influence of nanowire thickness is clear that PL counts for the nanowire with d = 90 nm are higher.

It was found that the intensity of the hot luminescence band reached a maximum at a resonant size of d = 90 nm, with a clear peak structure reflecting phonon-assisted hot luminescence processes. These are referred to as resonantly-sized cavities where the resonance is between high efficiency emission channels and the cavity modes. According to Agarwal et al. [5] the measurements was performed on plasmonically-coupled nanowires in the range of d = 30-80 nm and the photon counts of hot photoluminescence were highest for the nanowire with d = 70 nm. It is supposed that the origin of the efficient emission channels is related to the phonon dispersion of silicon.

4.1.4 Influence of SiO$_2$ oxide thickness on the photoluminescence spectrum

As previously described, the oxide layer of silicon (SiO$_2$) is used to separate the active silicon core from the silver. The devices were prepared with two different oxide layers. In this chapter, various samples with SiO$_2$ layer from thermal oxidation are tested and compared with each other.

Three PL spectra of a silicon nanowire device coupled with an Ω-shaped cavity (100 nm Ag film) and different oxide thickness are exemplary depicted in figure 4.7. The blue curve shows no PL of silicon nanowire without cavity.

Except the sample without the plasmonic cavity, all other nanowires show hot luminescence spectra with high counts. It can be seen in figure 4.7 that highest PL peak belongs to the nanowire with 5 nm oxide thickness.
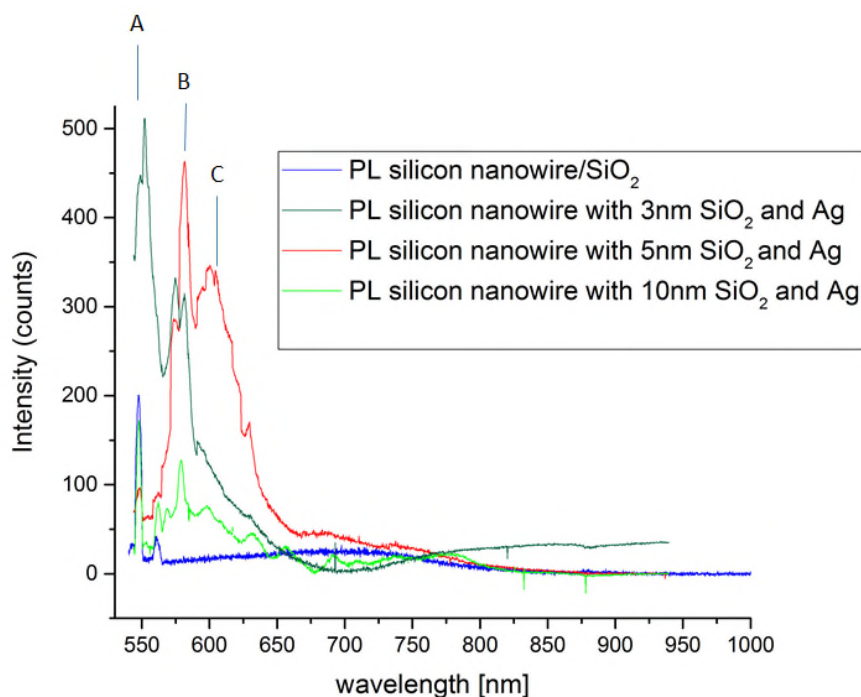

Figure 4.7: PL spectrum of bare silicon nanowire coated with ~ 5 nm SiO$_2$ only (blue) and PL spectra of Ω-cavity silicon nanowires devices coated with 3 nm/ 5 nm/ 10 nm SiO$_2$ interlayer and 100 nm Ag

The PL spectrum of the bare silicon nanowire (blue curve) shows a response at noise level as expected from bulk silicon. On the other hand, the spectra of the nanowires coupled with the plasmonic Ω-cavity reveal broad luminescence. The first peaks (A) at all PL measurements are around 549 nm and are assigned to silicon Raman peaks. Peaks B at wavelength of 582 nm present high counts obtained from the silicon nanowires coupled with an Ω-shaped cavity. The photon counts of hot PL were highest for the device with 5 nm thick SiO_2 dielectric layer. As previously described, oxide layer is used as an insulating interlayer to separate the active material from the metal and thereby prevent non-radiative recombination of charge carriers at the metal surface. [63] A very thin oxide at about 3 nm cannot perform exactly this goal. Besides the thin oxide layer, a device with a 10 nm thick SiO_2 layer was also fabricated. These plasmonically coupled silicon nanowires show very weak PL peaks and it can thus be explained that a thick oxide layer suppresses the plasmonic effects. The silicon nanowire device with a 5 nm thick oxide layer has additionally a distinct PL peak at a wavelength of 601 nm (C). That could be the further possible cavity mode.

4.1.5 Influence of silver layer quality

To investigate the influence of the Ag layer quality the silicon nanowires with 5 nm SiO_2 were coated by metallization of 100 nm of silver via two different methods, namely sputtering and electron beam evaporation. The different layer quality of sputtered and evaporated layers causes different PL spectra.

A silver thin film was coated the silicon nanowire to form an Ω-shaped plasmonic cavity by using an electron-beam evaporator. An Ω-shaped Ag layer can be reach only with an electron-beam evaporator.
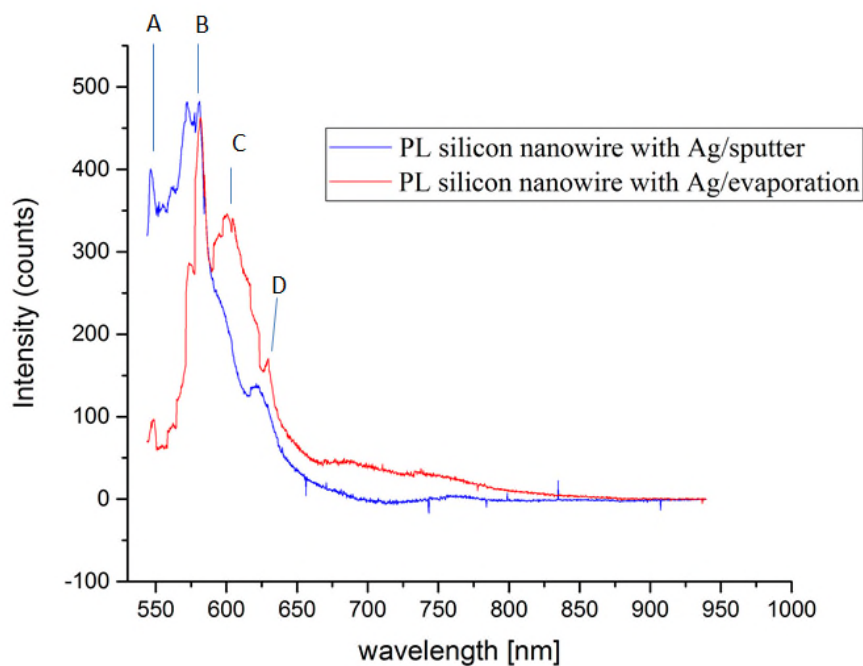

Figure 4.8: PL spectra from silicon nanowires devices with a 5 nm SiO_2 as interlayer coupled with an 100 nm *Ω*- shaped Ag cavity via two coating methods, namely vapor deposition (red) and sputtering (blue)

Figure 4.8 shows PL spectra from silicon nanowire devices coupled with an Ω-shaped cavity. The blue curve belongs to the device, which was coated with silver by vapor deposition and the red curve shows PL spectrum of the device with a sputtered silver layer. In both spectra the first peaks (A) at 545 nm correspond to the Raman peak of silicon. The emission peaks at approximately 577 nm, 600 nm and 625 nm denoted with B, C, D can be identified as emission from the plasmonics coupled nanowires. The PL peaks at 577 nm (B) show comparable emission intensities for both methods (evaporation and sputtering). The silicon nanowir with the sputtered Ag layer (blue curve) shows higher PL emission in the range between 550 nm and 575 nm compared to the sample with the evaporated Ag layer (red curve). For the sample with the evaporated Ag layer a pronounced emission peak close to 600 nm is visible, whereas the same wavelength position, the sample with the sputtered Ag layer only shows a hardly pronounced PL.

4.1.6 Influence of Al_2O_3 oxide thickness on the photoluminescence spectrum

As previously described, the samples were prepared with two different oxide layers. In this chapter, various samples with Al_2O_3 interlayer deposited by ALD are tested.

Figure 4.9 depicts the PL spectra of nanowires coupled with the plasmonic Ω-cavity with two different oxide thicknesses 3 nm and 5 nm.
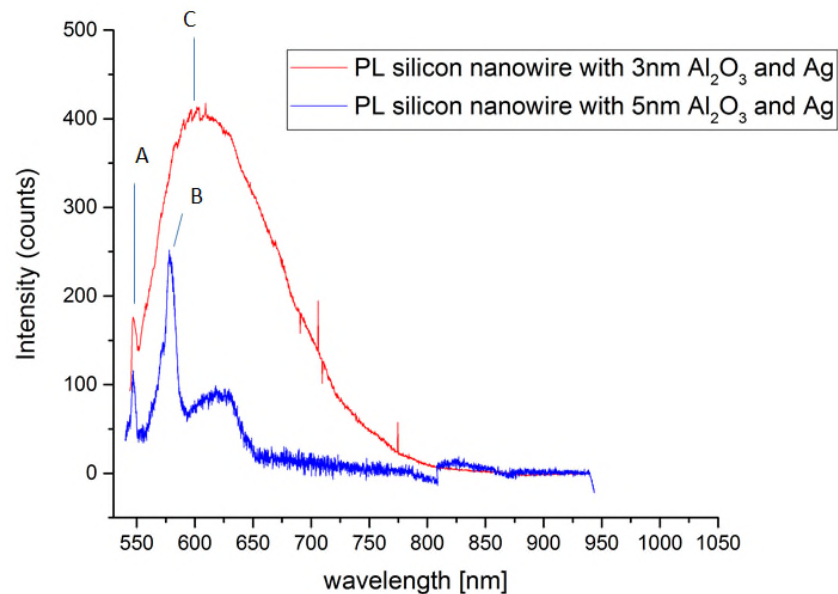

Figure 4.9: PL spectra measured from a silicon nanowire with 3 nm (red curve) and 5 nm (blue curve) thick Al_2O_3 layer and an about 100 nm thick Ag plasmonic Ω-cavity

The Raman peak denoted as A corresponds to the Raman peak of silicon. Peak B at 578 nm is a sharp peak of a plasmonically coupled nanowire in a device with 5 nm Al_2O_3. Peak C, on the other hand, is a rather broad peak with the center at 606 nm. In a direct comparison, it is found that when Al_2O_3 is used as the interlayer, a thickness of 3 nm is the ideal oxide thickness. The PL of this device clearly shows higher emission in the visible range.

4.1.7 Influence of silver layer thickness

Two silicon nanowires devices with 3 nm Al_2O_3 and different thicknesses of silver are investigated. As previously discussed, silver is the basis for supporting surface plasmon modes in the vicinity of the silicon core, which can span the visible spectral range. Interestingly, the emission is strongest for Ag cavities with a layer thickness of 50 nm. The different Ag layer thickness causes different PL spectra, as shown in the figure 4.10.
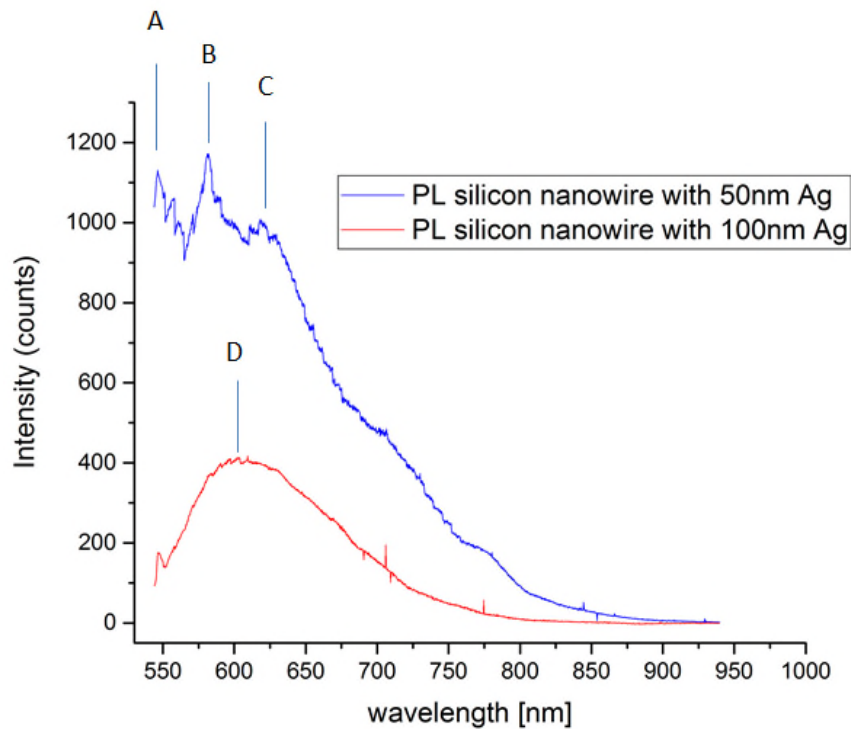

Figure 4.10: PL from silicon nanowires coupled to a plasmon nanocavity with 3 nm Al_2O_3 oxide layer thickness and a Ag layer thickness of 50 nm (blue) and 100 nm (red)

In both PL spectra, the first silicon Raman peaks are at 545 nm (A). The red curve shows a broad PL spectrum of a silicon nanowire with a 100 nm thick Ag cavity at center wavelength of approximately 604 nm. On the other hand, the silicon nanowire device coupled with a 50 nm Ag as a Ω-shaped cavity shows a very strong peak with two sharp peaks, which shows the metal nanocavity resonant modes. Peak B at 581 nm and peak C at 617 nm characterize the cavity enhanced hot luminescence of a plasmonically coupled silicon nanowire.

4.2 Raman spectroscopy

In all PL measurement results, there are two peaks that can be seen repeatedly. They occur approximately at a wavelength of about 545 nm and 560 nm. Raman spectroscopy was utilized, as described in section 3.3 with a power of 93 µW and integration time of 2x15 s. In the following, a basic description of the results by Raman inspection of the silicon nanowire and glass substrate will be given. Afterwards a discussion of Raman signals is presented.

To detect and understand the PL peaks from the bare silicon nanowire and the one with the plasmonic cavity, the Raman peaks of silicon and glass substrate were observed. All Raman spectra were calibrated by the Rayleigh peak position. Raman spectra were achieved at room temperatures and ambient laboratory conditions. Figure 4.11 shows an optical image of silicon nanowires on the glass substrate.
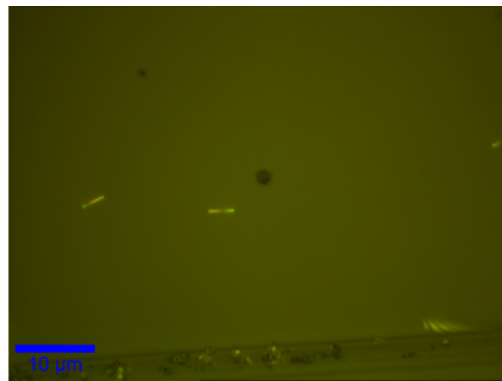

Figure 4.11: Optical image of silicon nanowire on the glass substrate

Figure 4.12 shows the reference Raman spectrum of glass (a) and silicon nanowire on glass substrate (b). The peak A is the Rayleigh peak. Peak C is the typical silicon Raman peak. The two broad peaks, B and D at 545 nm und 561 nm in the Raman measurement of glass and silicon nanowire were also observed in most of the PL measurements.
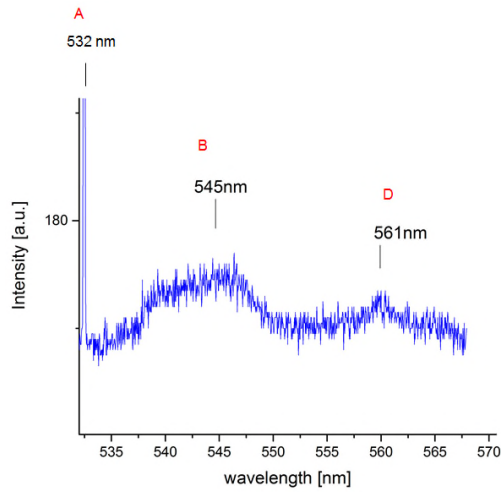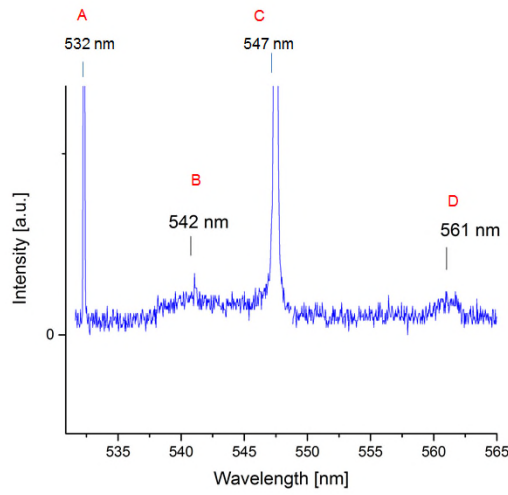
Figure 4.12: Raman spectrum of (a) the glass substrate and (b) silicon nanowire on glass substrate

Comparison of spectra with data presented by Khorasaninejad et al., where the Raman spectra from bulk silicon and nanowire samples was investigated, would suggest a Raman peaks for the silicon nanowire in the range of 100 to 1000 rel cm^{-1}. According to Khorasaninejad the Raman spectrum of bulk crystalline silicon has been studied and is understood, possessing only one Raman active first-order phonon, that centered in the Brillouin zone, with an optical phonon energy of 520 cm^{-1}. [64]
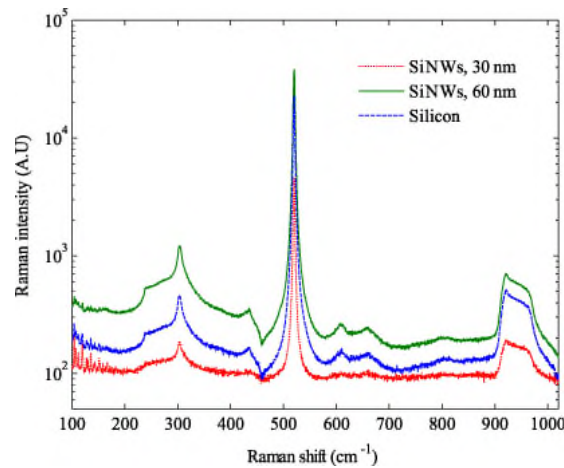
Figure 4.13: Raman spectra from bulk silicon and nanowire samples of 30 and 60 nm diameters [64]

4.3 PL investigation on strain silicon nanowire integrated in plasmonic nanocavity

In this chapter the silicon nanowire coupled with a plasmon nanocavity is tested on a MEMS straining device. The nanowires and device used in this part of work were synthesized and fabricated by Dipl. Ing. Dr. Stefan Wagesreither. The ultimate goal was to achieve bright light emission from mechanically strained silicon nanowires integrated in a MEMS device, as explained in chapter 3.4.

Silicon nanowire was monolithically integrated in the gap between the stage and specimen part. First, these specific nanowires are measured. Then a 4 nm Al_2O_3 layer as oxide layer via ALD is added. As a next step, a 100 nm Ag is deposited. After Ag deposition, the sample is measured. By performing line scans along a strained nanowire with the micro-Raman spectroscopy setup 3.3.2 the spatial resolved strain mapping of the nanowire can be achieved before PL measurement. Figure 4.14 shows the SEM-image of device structure.
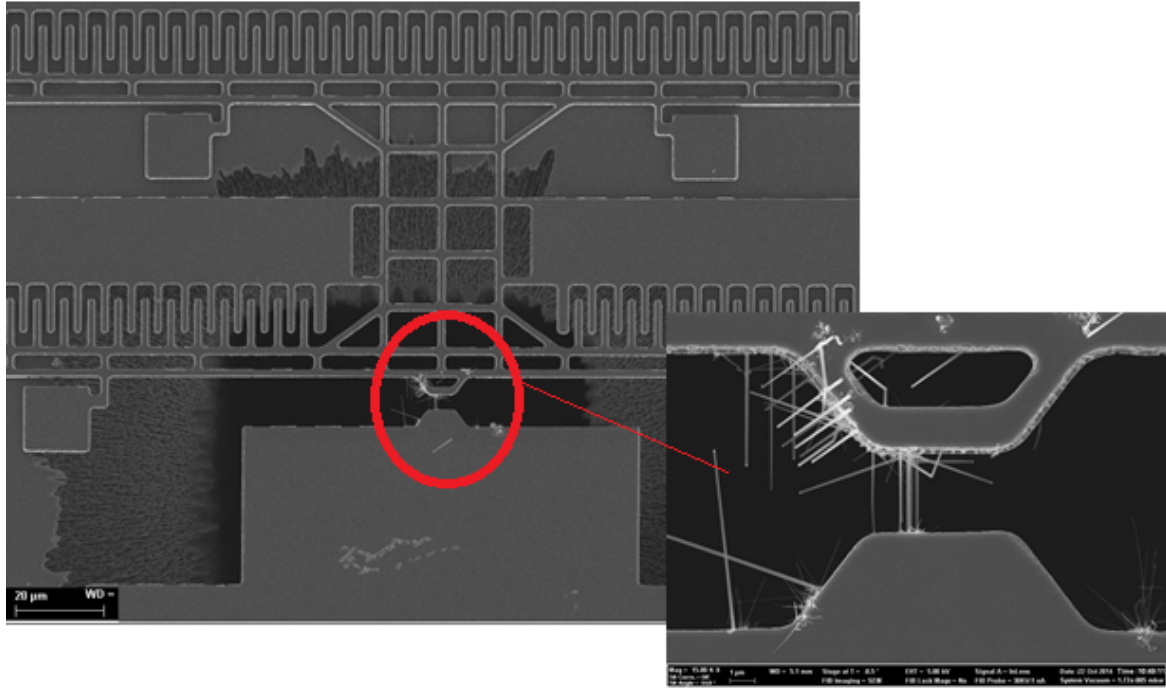
Figure 4.14: SEM image of a MEMS device. Silicon nanowire integrated in the gap between the stage and specimen. Through the hole behind the device, the required layers are incensed to fabricate the silicon nanowire with the plasmonic cavity.

Figure 4.15 presents the PL spectra of the silicon nanowire introduced in the MEMS device. As it was expected, there is negligible emission for the nanowire without the plasmonic cavity (blue curve). However, the silicon nanowire coupled with an Ω-shaped cavity on the device demonstrates a broad PL peak and distinct peaks at about 570 nm (red curve).
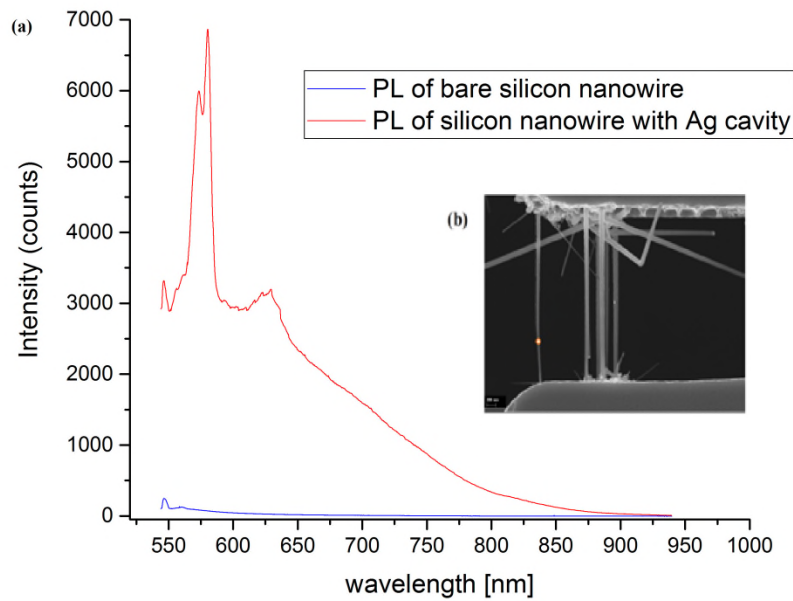
Figure 4.15: (a) PL spectrum of bare silicon nanowire (blue curve) and the same Ω-cavity nanowire with 4 nm Al_2O_3 and 100 nm Ag (red curve), (b) The SEM image of measured nanowire. The measurement point is marked in the SEM image in the inset

Previous to the straining experiments the MEMS supporting silicon beams fixing stage during processing will be removed by FIB cutting. After the removal of the supporting beams the stage part is fully movable but the device is from now on incompatible to any kind of wet processes (figure 4.16). In order to support the mobility of device, all other nanowires except for measured cavity nanowire between the stage and specimen part will be cutting by FIB.
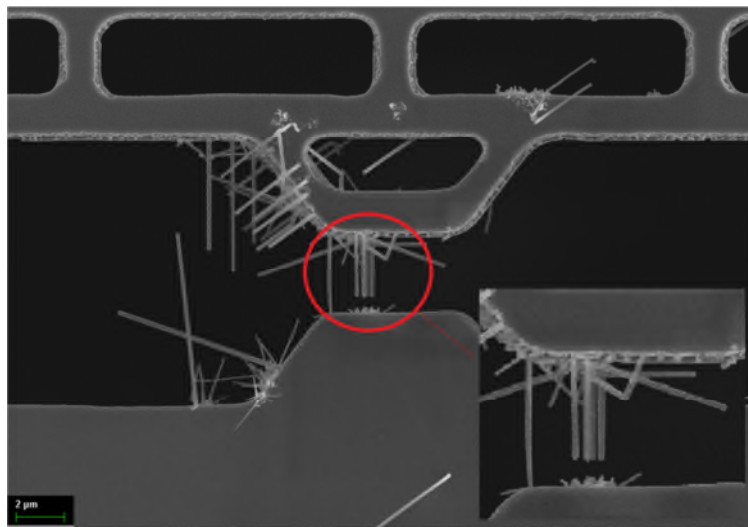

Figure 4.16: SEM image of MEMS device after FIB cutting of parasitic silicon nanowires between the stage and specimen part

By applying a voltage on the actuator part, electrostatic forces pull the freestanding cantilever of the stage towards the actuator part thus straining the suspended silicon nanowire. [61]

Figure 4.17 shows the Raman spectra of the silicon nanowire for different actuator voltages. As clearly shown in the inset, with increasing voltage, the first order zone center silicon Raman peak shifts to lower wavenumbers.
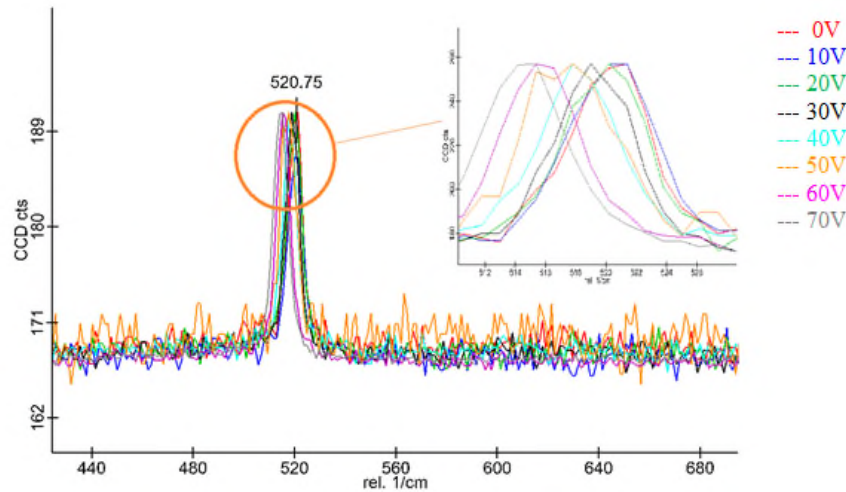

Figure 4.17: Silicon Raman peak of a silicon nanowire in the MEMS device between the stage and specimen part as function of the actuator voltage

The peak shifts are compared with the absolute physical length change of the nanowire for different actuation voltages to calibrate the Raman measurements with respect to nanowire elongation. Thereby, the relation of the Raman peak shift and uniaxial strain is given by [61]

$$\Delta\Omega = k \cdot \varepsilon$$

with $\Delta\Omega$ representing the shift in the Raman peak position, k a proportionality factor, and ε the strain along the $\langle 111 \rangle$ growth direction of the VLS grown silicon nanowire. $K = 333$ cm^{-1} for calibration measurements can be used to calculate the ε in dependence to voltage up to 80V. Figure 4.18 demonstrates the proportionality of strain and the applied actuator voltage.
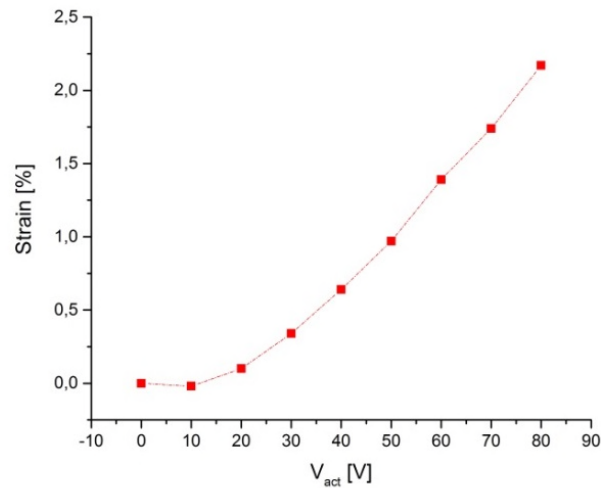
Figure 4.18: Calculated strain generated by the MEMS applied on cavity silicon nanowire as a function of the actuator voltage V_{act}

Thus, an actuator voltage of 80 V leads to a peak shift and to a tensile strain of about 2.17%.

To characterize the PL response of the silicon nanowire integrated in the MEMS device of different strain level a DC-voltage was applied on the specimen part from V = 10 V to 100 V and monitored the PL spectra in the nanowire at different actuator voltages. Thereby the stage and the handle layer of the substrate were grounded to avoid electrostatic attraction between the movable cantilever of the stage part and the substrate. To avoid a possible fracture of the nanowire due to an instant high strain level, the actuator voltage was ramped up in steps of 5 V.

Figure 4.19 shows PL spectra of the suspended silicon nanowire for different actuator voltages and therefore strain levels. This figure presents that the PL spectra of plasmonic silicon nanowire become weaker under strain. The bandgap shift of silicon under strain is believed to cause the change of the PL spectra of silicon. [65]
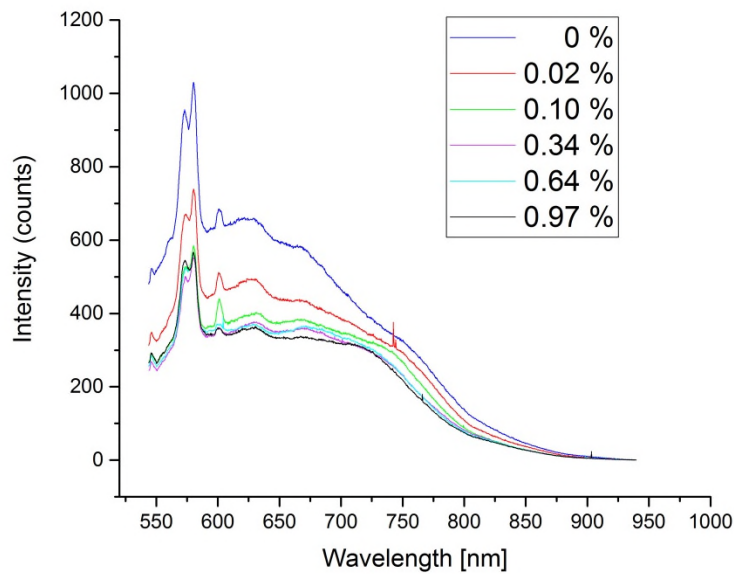
Figure 4.19: PL peak shift depending on strain. Hot luminescence from silicon nanowire coupled to a plasmon nanocavity with 4 nm thick Al_2O_3 interlayer and 100 nm Ag cavity in a MEMS device for various actuator voltages from 0 V to 50 V

Instant release from 50 V to 0 V has shown no damage on the nanowire and the PL showed a complete return to the original unstrained. Afterwards the voltage is increased up to 100 V, as seen in figure 4.20; over 60 V sinking the PL can be detected. In the step after 100 V nanowire is broken off. Figure 4.20 shows a SEM image of broken silicon nanowire integrated on a MEMS.

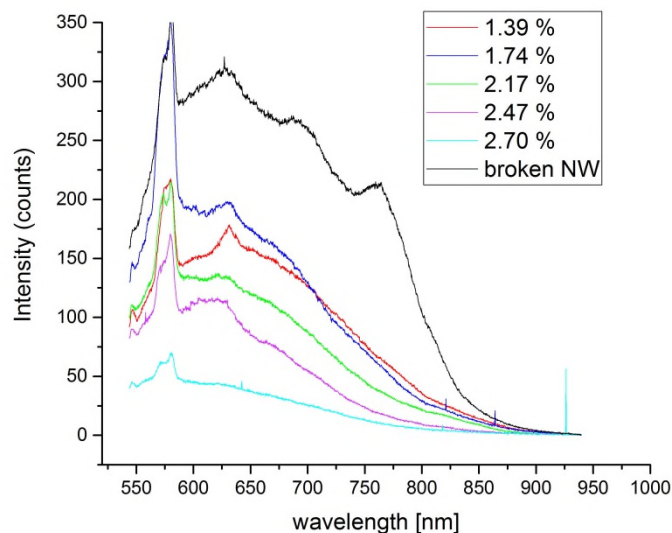
Figure 4.20: PL peak shift depending on strain. Hot luminescence from silicon nanowire coupled to a plasmon nanocavity with 4 nm thick Al_2O_3 interlayer and 100 nm Ag cavity in a MEMS device for various actuator voltages from 60 V to 100 V

54

As shown in the previous figure, the PL spectra of silicon nanowires with cavity change when applying strain. In this part, the actuator voltage is varied from 60 V to 100 V. In contrast to lower actuator voltages until 50 V, no regular changes of PL are observed here.

Following the PL changes of silicon nanowire under strain to 0.97% a reduction of PL spectra as a function of strain between 1.3% and 2.7% is expected. But as shown in figure 4.20, there is an increase of the overall PL under strain of 1.39% to 1.74% and then further decrease of PL spectra up to strain levels of 2.7%. For these results, no precise explanation was found in this work.
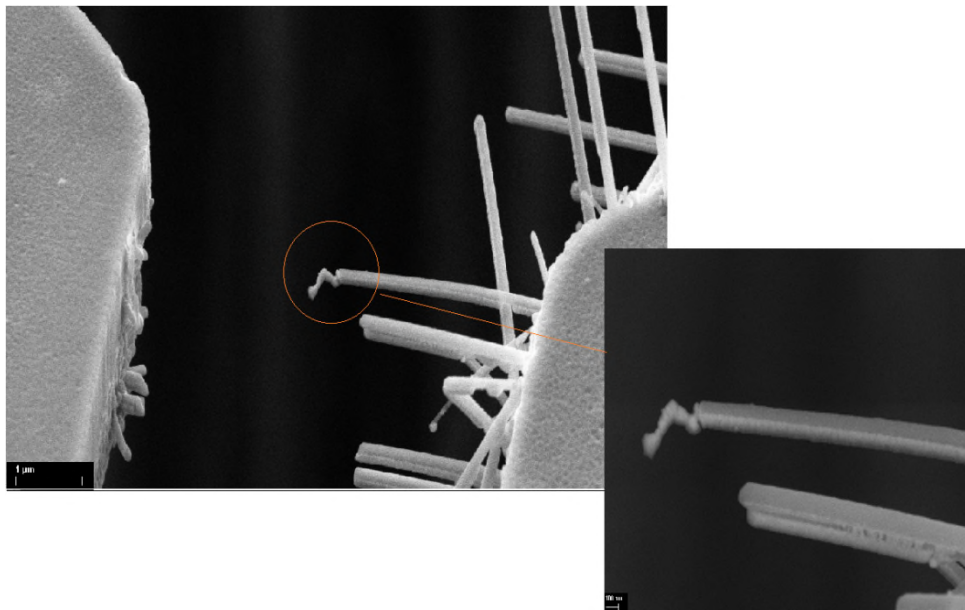

Figure 4.21: SEM image of broken nanowire after strain with actuator voltage 100 V under 2.7 % strain

5. Conclusion and outlook

Since the early demonstration of cavity enhanced spontaneous emission in 1983 [66], there has been a tremendous advance in applying dielectric microcavities for enhanced light matter interaction for quantum optics. Recently, more attention has been drawn to the development of plasmonic nanocavities for their ability to confine light within sub-wavelength dimensions and thereby achieve significant enhancement of spontaneous emission.

The ability to obtain visible light emission from silicon devices is important for possible integration with active silicon based photonics. In this thesis, the design and fabrication of a type of plasmonic cavities was demonstrated. This method offers a way to obtain light emission from any indirect bandgap semiconductor and will be useful for the fabrication of monolithic devices utilizing optics for ultrafast data processing. [5]

The goal of this thesis is investigating how the optical properties of silicon nanowires integrated with a plasmonic cavity change as compared to those without cavity effect. The thesis is organized as follows. After a short introduction in chapter one, chapter two treats a wide spectrum of theoretical backgrounds of the work. The properties of silicon nanowires and photoluminescence, weak and strong coupling were experimentally studied.

Chapter three takes attention on the experimental procedures used for this work, as well as the used equipment and the measurement setup. A fabrication method developed to fabricate silicon nanowires with plasmonic effect is described.

To understand the interaction of silicon phonon modes and nanocavity plasmon resonances leading to efficient light emission, photoluminescence measurements were carried out. Finally chapter four embraced all measurements and experiments and discussed the results. These observations suggest that the hot carriers emit photons through a phonon assisted recombination process during intraband relaxation.

Engineering light emission from silicon has been of great interest for developing efficient silicon-based light sources, which can be easily integrated with conventional electronics. It has been known that silicon emits visible light only when it forms quantum-confined nanostructures at sub-10 nm length scales. [67] However, there are difficulties in integrating quantum structures with conventional electronics. [68] In this work, according to Agarwal et al. [5] an entirely new concept was demonstrate to achieve bright visible light emission in "bulk-sized" silicon coupled with a plasmon nanocavity at length scales that are compatible with current electronic devices (80−130 nm). Highly concentrated electromagnetic field supported by the plasmon nanocavity generates bright visible light emission from non-thermalized hot carriers before the relaxation of the hot carriers. The rapid recombination of hot carriers before their relaxation is due to the large Purcell enhancement in these plasmonic nanocavities. [5] The enhanced emission quantum efficiency at room temperature in plasmonic silicon, along with its size compatibility with present silicon electronics, provides new avenues for the development of a monolithically integrated light-source on conventional microchips.

List of abbreviations

Al_2O_3	Aluminum Oxide
ALD	Atomic Layer Deposition
Ar	Argon
Au	Gold
BHF	Buffered Hydrofluoric Acid
c-Si	Crystalline Silicon
CCD	Charge-Coupled Device
CVD	Chemical Vapor Deposition
DI water	De-Ionized water
EASD	Electrostatic Actuated Straining Device
EBAE	Electron-beam Assisted Evaporation
EM	Electromagnetic
FET	Field Effect Transistor
FIB	Focused Ion Beam
LDOS	Local Density of States
LPCVD	Low Pressure Chemical Vapor Deposition
LSPR	Localized Surface Plasmon Resonance
MEMS	Micro Electro Mechanical System
ND:YAG	Neodym-Dotierter Yttrium-Aluminium-Granat
NI	Near Infrared
NW	Nanowire
NP	Nanoparticle
PECVD	Plasma Enhanced Chemical Vapor Deposition
PhD	Doctor of Philosophy
PL	Photoluminescence
PVD	Physical Vapor Deposition
RTA	Rapid Thermal Annealing
SD	Sputter Deposition
SEM	Scanning Electron Microscopy
Si	Silicon
SiO_2	Silicon Dioxide
SPP	Surface Plasmon Polaritons
TE	Transverse Electric
TM	Transverse Magnetic
VLS	Vapor-Liquid-Solid
UV	Ultraviolet
WD	Working Distance

Bibliography

[1]. R. Zia, J. A. Schuller, A. Chandran, M. L. Brongersma. Plasmonic: the next chip-scale technology, Materialstoday, 9, 20, 2006.

[2]. K. Banerjee, A. Amerasekera, G. Dixit, C. Hu. The effect of interconnect scaling and low-k dielectric on the thermals characteristics of the IC metal, IEEE, 65, 1996.

[3]. Bulk Silicon Emits Visible Light, http://www.photonics.com/Article.aspx?AID=53424, 2013.

[4]. M. L. Brongersma, R. Zia, and J. Schuler. Plasmonics: the Missing Link between Nanoelectronics and Microphotonics, Piers online, 3, 360, 2007.

[5]. C. H. Cho, C. O. Aspetti, J. Park, R. Agarwal. Silicon coupled with plasmon nanocavities generates bright visible hot luminescence, Nature photonics, 7, 285, 2013.

[6]. A glimmer of light from silicon, http://spectrum.ieee.org/semiconductors/optoelectronics/a-glimmer-of-light-from-silicon, 2013.

[7]. Light from silicon, https://spectrum.ieee.org/semiconductors/processors/light-from-silicon, 2005.

[8]. C. E. Hofmann. Optics at the Nanoscale: Light Emission in Plasmonic Nanocavities, PhD-Thesis, California Institute of Technology, 2010.

[9]. B. A. Manhat. Understanding the emission from semiconductor nanoparticles, PhD-Thesis, Portland State University, 2012.

[10]. Y. Kanemitsu. Light-emitting silicon materials, Journal of luminescence, 70, 333, 1996.

[11]. A. G. Cullis, L. T. Canham, P. D. J. Calcott. The structural and luminescence properties of porous silicon, Applied physics reviews, 82, 909, 1997.

[12]. P. Bai, H. S. Chu, M. Gu, O. Kurniawan, E. Li. Integration of plasmonics into nanoelectronic circuits, Physica B: condensed matter, 405, 2978, 2010.

[13]. G. Audoit, É. Mhuircheartaigh, S. Lipson, M. Morris, W. Blaub, J. Holmes. Strain induced photoluminescence from silicon and germanium nanowire arrays, Journal of materials chemistry, 15, 4809, 2005.

[14]. A. A. Hadi. Enhancement of porous silicon Formation by Using laser Irradiation, Engineering and technology journal, 31, 348, 2013.

[15]. Silicon, http://nautilus.fis.uc.pt/st2.5/scenes-e/elem/e01410.html

[16]. N. Storey, Electronics: A systems Approach, ISBN: 9780273719182, 2009.

[17]. J. Singh. Semiconductor devices: basic principles, ISBN: 9780471362456, 2001.

[18]. L. Mui, Y. Changi, S. D. Sawtelle, M, Wipf, X. Duani, M. A. Reed. Silicon Nanowire Field-Effect Transistors-A Versatile Class of Potentiometric Nanobiosensors, Access, 3, 2422842, 2015.

[19]. L. Tsakalakosa, J. Balch, J. Fronheiser, B. A. Korevaar. Silicon nanowire solar cells, Applied physics letters, 91, 233117, 2007.

[20]. J. Westwater, D. P. Gosain, S. Tomiya, S. Usui, H. Ruda. Growth of silicon nanowires via gold/silane vapor-liquid-solid reaction, Journal of vacuum science & technology, 15, 554, 1997.

[21]. S. Wagesreither. Strain Engineering in Intrinsic Silicon Nanowires using MEMS Devices, PhD-Thesis, Technischen Universität Wien, 2015.

[22]. Chapter 12: Electrical Properties, http://people.clarkson.edu/~isuni/Chap-12.pdf, 2010.

[23]. H. Föll. Semiconductor – Script, Doping and Mobility, http://www.tf.uni-kiel.de/matwis/amat/semi_en/kap_2/illustr/i2_2_3.html

[24]. P. Laube, Semiconductor Technology, https://www.halbleiter.org/en/fundamentals/doping/

[25]. R. Wittmann. Miniaturization Problems in CMOS Technology: Investigation of Doping Profiles and Reliability, PhD-Thesis, Technischen Universität Wien, 2007.

[26]. Direct and Indirect Band Gap Semiconductors, https://www.doitpoms.ac.uk/tlplib/semiconductors/direct.php, 2004.

[27]. T.K. Bergstrasser, M. L. Cohen. Band Structures and Pseudopotential Form Factors for Fourteen Semiconductors of the Diamond and Zinc-blende Structures, Physical review, 141, 789, 1966.

[28]. T. V. Arguirov. Electro-optical properties of dislocations in silicon and their possible application for light emitters, PhD-Thesis, Technischen Universität Cottbus, 2007.

[29]. D. Bliman. Purine and Pyrazolopyrimidine Derivatives Design and Synthesis of Chemical Tools for Biological Applications, Phd-Thesis, University of Gothenburg, 2015.

[30]. S. Mukherjee, Applied Mineralogy: Applications in Industry and Environment, ISBN: 978-94-007-1161-7, 2011.

[31]. S. Doka Yamigno. Characterization of as-grown and Ge - ion implanted CuGaSe2 thin films prepared by the CCSVT technique, PhD-Thesis, Berlin, 2007.

[32]. D. R. Vij. Luminescence of Solids, ISBN: 0-306-45643-5, 1998.

[33]. A. Kitzler. Electrical and Electro-optical Characterization of Novel Si/GaAs Nanowire Heterostructures, Master Thesis, Technischen Universität Wien, 2015.

[34]. K. K. Smith, Photoluminescence of semiconductor materials, Thin solid films, 84, 171, 1981.

[35]. H. Atwater. The promise of plasmonics, Scientific american, 296, 56, 2007.

[36]. H. P. Wagner, M. K. Baghbadorani. Plasmonics: Revolutionizing light-based technologies via electron oscillations in metals, https://theconversation.com/plasmonics-revolutionizing-light-based-technologies-via-electron-oscillations-in-metals-38697, 2015.

[37]. M. Fox, Optical Properties of Solids, ISBN 978-0-19-850613-3, 2003.

[38]. L. Barnes, A. Dereux, T. W. Ebbesen. Surface plasmon subwavelength optics, Nature, 424, 824, 2003.

[39]. M. Liu, X. Zhang. Nano-optics: Plasmon-boosted magneto-optics, Nature photonics, 7, 429, 2013.

[40]. B. Rothenhäusler, W. Knoll. Surface plasmon microscopy, Nature, 332, 615, 1988.

[41]. S. Pillaia, K. R. Catchpole, T. Trupke, M. A. Green. Surface plasmon enhanced silicon solar cells, Journal of applied physics, 101, 093105, 2007.

[42]. W. L. Barnes, A. Dereux, and T. W. Ebbesen. Surface plasmon subwavelength optics, Nature, 424, 824, 2003.

[43]. Y. Ma. Surface Plasmon Polaritons based Nanophotonic Devices and their Applications, PhD-Thesis, Dublin Institute of Technology, 2015.

[44]. S. A. Maier. Plasmonics: Fundamentals and Applications, ISBN: 9780387331508, 2007.

[45]. J. Zhang, L. Zhang, W. Xu, Surface plasmon polaritons: physics and applications, Journal of physics D: applied physics, 45, 113001, 2012.

[46]. C. C. Klick, J. H. Schulman. Luminescence in Solids, Academic press, 5, 97, 1957.

[47]. Collection Mémoires et thèses électroniques, Surface plasmon polaritons: theoretical framework, http://theses.ulaval.ca/archimede/fichiers/24879/ch05.html, 2007.

[48]. K. Y. Kim. Plasmonics - Principles and Applications, ISBN: 978-953-51-0797-2, 2012.

[49]. K. J.Vahala. Optical microcavities, Nature, 424, 839, 2003.

[50]. A. A. Toropov, and T. V. Shubina. plasmonic Effects in Metal-Semiconductor Nanostructures, ISBN: 978-0-19-969931-5, 2015.

[51]. E.M. Purcell. Spontaneous emission probabilities at radio frequencies, Physical review, 69, 681, 1946.

[52]. V. Giannini, A. I. Fernandez-Domínguez, S. C. Heck, Stefan A. Maier. Plasmonic Nanoantennas: Fundamentals and Their Use in Controlling the Radiative Properties of Nanoemitters, Chemical reviews, 111, 3888, 2011.

[53]. J. D. Jackson. Classical Electrodynamics, ISBN: 978-0471309321, 1999.

[54]. P. R. Berman. Cavity Quantum Electrodynamics, Academic press, ISBN: 9780120922451, 1994.

[55]. T. L. Liu. Plasmonic Cavities for Enhanced Spontaneous Emission, PhD-Thesis, Harvard University, 2013.

[56]. L. Novotny, and B. Hecht, Principles of Nano-Optics, ISBN: 9780511813535, 2006.

[57]. L. Vivien, L. Pavesi. Handbook of Silicon Photonics, ISBN 978-1-4398-3611-8, 2013.

[58]. A. Lugstein, Y. J. Hyun, M. Steinmair, B. Dielacher, G. Hauer, E. Bertagnolli. Some aspects of substrate pretreatment for epitaxial Si nanowire growth, Nanotechnology, 19, 485606, 2008.

[59]. C. D. Travis, R. A. Adomaitis. Dynamic Modeling for the Design and Cyclic Operation of an Atomic Layer Deposition (ALD) Reactor, Processes, 1, 128, 2013.

[60]. WITec Wissenschaftliche Instrumente und Technologie GmbH. alpha300 System Description, 2008.

[61]. S. Wagesreither, E. Bertagnolli1, S. Kawase, Y. Isono, A. Lugstein. Electrostatic actuated strain engineering in monolithically integrated VLS grown silicon nanowires, Nanotechnology, 25, 455705, 2014.

[62]. C. O. Aspetti. Surface Plasmon Based Engineering of Semiconductor Nanowire Optics, PhD-Thesis, University of Pennsylvania, 2014.

[63]. C. O. Aspetti, C. Cho, Ra. Agarwal, Ri. Agarwal. Studies of hot photoluminescence in plasmonically coupled silicon via variable energy excitation and temperature dependent spectroscopy, Nano letters, 14, 5413, 2014.

[64]. M. Khorasaninejad, J. Walia, S. Saini. Enhanced first-order Raman scattering from arrays of vertical silicon nanowires, Nanotechnology, 23, 275706, 2012.

[65]. J. Cai, Y. Ishikawa, K. Wada. Strain induced bandgap and refractive index variation of silicon, Optics express, 21, 7162, 2013.

[66]. P. Goy, J. M. Raimond, M. Gross, S. Haroche. Observation of cavity-enhanced single-atom spontaneous emission, Physical review letters, 50, 1903, 1983.

[67]. A. G. Cullis, L. T. Canham, Visible light emission due to quantum size effects in highly porous crystalline silicon, Nature, 353, 335, 1991.

[68]. R. J. Walters, G. I. Bourianoff, H. A. Atwater. Field-effect electroluminescence in silicon nanocrystals, Nature materials, 4, 143, 2005.